Journal of
Manufacturing and Materials Processing

MDPI

Review

A Comprehensive Review of High-Pressure Laser-Induced Materials Processing, Part II: *Laser-Driven Dynamic Compression within Diamond Anvil Cells*

Mohamad E. Alabdulkarim, Wendy D. Maxwell, Vibhor Thapliyal and James L. Maxwell *

EεMC^2 Labs, Department of Engineering, La Trobe University, Bendigo, VIC 3550, Australia
* Correspondence: j.maxwell@latrobe.edu.au

Abstract: The field of high-pressure materials research has grown steadily over the last seven decades, with many remarkable discoveries having been made. This work is part II of a three-part series summarising recent progress in *laser* material processing within *diamond anvil cells* (L-DACs); this article focuses on the practice of *laser-driven dynamic compression* within diamond anvil cells (i.e., *LDC–DAC* experimentation). In this case, materials are initially pre-compressed within diamond anvil cells, then further dynamically compressed through the use of a high-power pulsed laser, often with the intent to isentropically compress, rather than to heat samples. The LDC–DAC approach provides a novel route to much higher dynamic pressures (approaching 1 TPa), as compared to conventional static compression within a single-stage DAC (<300 GPa) and provides a route to mapping Hugoniot curves. Recent proliferation of low-cost, high-power laser sources has led to increased research activity in LDC–DAC materials processing over the last two decades. Through LDC–DAC experiments, a greater understanding of the properties/structure of cold- and warm-dense matter has been obtained, and novel material phases have been realised. In this article, LDC–DAC experimental methods are reviewed, together with the underlying physics of laser dynamic compression in confined spaces. In addition, a chronology of important events in the development of LDC–DAC processing is provided, and emerging trends, gaps in knowledge, and suggestions for further work are considered.

Keywords: laser dynamic compression; diamond anvil cell; isentropic compression; shock wave; pressure wave; high pressure

Citation: Alabdulkarim, M.E.; Maxwell, W.D.; Thapliyal, V.; Maxwell, J.L. A Comprehensive Review of High-Pressure Laser-Induced Materials Processing, Part II: *Laser-Driven Dynamic Compression within Diamond Anvil Cells*. *J. Manuf. Mater. Process.* **2022**, *6*, 142. https://doi.org/10.3390/jmmp6060142

Academic Editor: Steven Y. Liang

Received: 10 October 2022
Accepted: 8 November 2022
Published: 14 November 2022

1. Introduction

Since the 1930's, investigators have developed increasingly capable pressure generating devices, such as lever-arm presses [1], piston-driven presses [2], and opposed anvil presses [3,4]; this has enabled materials to be studied at successively higher static pressures over time [5]. In the mid-20th century, Charlie Weir et al. invented the first ***diamond anvil cell (DAC)***, in which samples were observed directly through diamond anvils at pressures of over 3 GPa [6]; this revolutionised high pressure materials research, making it possible to monitor phase changes and chemical reactions as pressure was applied [6]. Soon thereafter, laser beams were introduced into DACs for the first time (to process materials) by Takahashi and Bassetta [1].

An apparatus that focuses a laser beam between diamond anvils to heat, shock, or induce chemical reactions within a sample, is known as a ***laser diamond anvil cell (L-DAC)*** [7]. L–DAC systems have opened a door to entirely new research fields, such as the measurement of material properties at high pressures and high temperatures (HPHT) [8–14] or the study of extremophile biological organisms at pressures similar to those extant at hydrothermal vents [3,15]. Figure 1A illustrates how the number of journal articles involving L–DAC experiments has risen steadily since the early 1990's—and is now approaching 60–70 articles per year (blue curve).

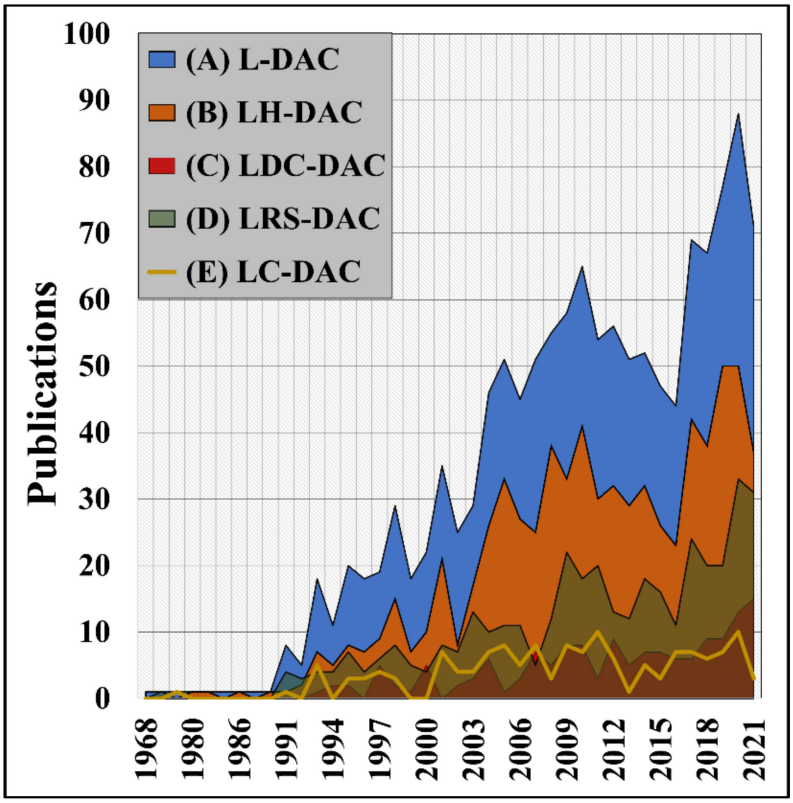

(**A**)

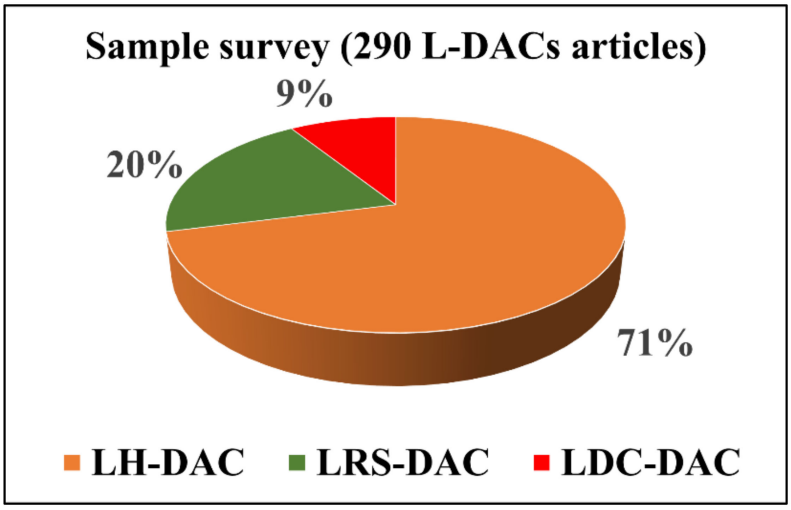

(**B**)

Figure 1. (**A**) Total annual scientific production for all L–DAC studies [Blue] compared with laser heated DAC (LH–DAC) [Orange], laser reactive synthesis DAC (LRS-DAC) [Green], and laser-driven dynamic compression DAC (LDC–DAC) [Red] studies [7]. (**B**) Comparison of the total number of articles produced in each.

The three parts of this review are based on the primary modes of material modification presented in Figure 1A,B. Part I of this series summarises the more common ***laser-heated diamond anvil cell (LH–DAC)*** mode of experimentation (71% of papers) [7]. This paper (Part II) focuses on *dynamic material compression* within DACs using intense pulsed lasers, rather than laser *heating* samples. We refer to this as ***laser-driven dynamic-compression diamond anvil cell (LDC–DAC)*** experimentation (9% of papers). The LDC–DAC mode

is distinguished from other L–DAC modes through the presence of a pressure-wave or shockwave that considerably modifies a sample material's structure/composition, and where heating is a *secondary* contributor, if present at all. Part III reviews the application of lasers to *induce chemical reactions* within diamond anvil cells (20% of papers); this latter method is dubbed ***laser reactive synthesis diamond anvil cell (LRS-DAC)*** experimentation. Although noteworthy reviews have previously outlined the development of DACs and high pressure research methods [1,5,6,14,16–18], this review speaks to *laser materials processing—where all three modes* of material modification/synthesis are described [19,20]. While the LH–DAC mode has been a principal driver throughout early L–DAC research [1], applications have now diversified, and interest is shifting toward the LDC–DAC and LRS-DAC modes—as evidenced by the **Red**/**Green** plots of Figure 1A.

This article (Part II), provides the key physics, historical events, and recent developments of LDC–DAC experimentation. Tables of materials modified/synthesised via LDC–DAC systems are given along with their corresponding process conditions of static pressure, shock pressures, temperature rises, and laser source wavelengths/energies (where available). Our intent is for the article to act as a field guide for others in setting-up and conducting their own high-pressure LDC–DAC research endeavours. Note that only laser-induced dynamic compression *within DACs* is considered here; neither light-gas gun experiments (without driving lasers) nor laser-induced shock compression (without transparent anvils) will be discussed in this review.

As further evidenced in this article, *LDC–DAC* experimentation provides researchers with a singular route to attaining extreme pressures across a large cross-sectional area (with pressures up to 1 TPa, thus far); the method is especially interesting as a *multiplicative* effect between the DAC pre-compression and the ***laser dynamic compression (LDC)*** has been documented [21]. This is well beyond the pressures attainable with single-stage hydrostatic or gas-membrane-driven diamond anvil cells [20,22] where otherwise multiple stages and/or nano-scale surface areas are required to attain such pressures [23].

LDC–DAC experimentation has enabled condensed matter physicists to determine material densities, melting curves, Hugoniot curves, equations of state (EOS), and transport properties for many common elements and compounds over a wide variety of conditions [19,20,24–27]. Furthermore, LDC–DAC methods have enabled geophysicists and planetary physicists to determine the properties of dense matter at conditions akin to those deep within planetary interiors, providing insight into the structure and dynamics present within the terrestrial planets [19,28]. The technique has allowed researchers to better understand how lasers interact with matter—and how shock-/pressure-waves travel through materials at high pressures [27,29]. Although *multi-stage* DACs can achieve pressures greater than 380 GPa, when sample sizes greater than 20 μm across are to be compressed, the LDC–DAC mode is presently the primary means to achieve pressures >> 380 GPa [19,30–32].

Alternative methods similar to, but distinguished from LDC–DAC processing are confined laser shock compression (e.g., explosive compression inside crystals) [33,34], open-atmosphere laser-driven dynamic compression (OA–LDC) [32,35], and high-power, multi-beam, laser-driven dynamic compression (HP–MB–LDC) [36,37]; all of these methods are generally conducted without the use of pre-compression within a diamond anvil cell, so they are excluded from this review. However, it is important to note that materials processing has indeed been carried out using these methods. For example, in the latter case (HP–MB–DC), the world's highest-ever recorded pressures while synthesising novel materials was achieved (≈1.5 and 5 TPa) and high-pressure forms of Si–C and diamond were realised [37,38]. Even greater pressures have been achieved by HP–MB–DC methods (to 100 TPa) during plasma fusion experiments, but without synthesising any intended material [39,40]. However, OA–LDC and HP–MB–LDC methods typically require large facilities with multiple laser sources, e.g., the National Ignition Facility (NIF) or OMEGA Laser Facility [30], which have traditionally been outside the scope of many researchers. That said, the availability of high-peak-power lasers is growing rapidly, with new capabilities in short-laser pulse lasers becoming widely accessible at a reasonable cost [41–44].

2. Methodology

This LDC–DAC review was performed using the research databases Web of Science®, ScienceDirect®, ProQuest Science®, SCOPUS®, Wiley Online Library®, IEEE Xplore®, Access Engineering®, and Google Scholar®. An initial search (within the title, keywords, and abstract) for the words, "diamond anvil cell," with no restrictions on publication date, generated over 8400 articles. Adding the keyword "laser" reduced this list to 1466 publications, starting in 1968 when the first L–DAC experiment was performed [45]. Results were then down-selected to 321 research papers directly pertaining to ***materials processing within diamond anvil cells***. Finally, using the keywords "diamond anvil cell" and "laser," combined with at least one of: "shock*," "pressure wave," or "dynamic compression," yielded 150 articles. A summary of all keywords searched are provided in Appendix A, Table A1. In addition to the listed keywords, key authors and research groups were also searched forward/backward in time to obtain additional articles. Finally, a variety of alternative keywords were searched to ensure that the database was comprehensive. From this, we were able to identify 27 works directly performing LDC–DAC experiments, where a laser-induced impulse was passed through a pre-compressed sample within a DAC.

3. Overview of Laser Dynamic Compression in Diamond Anvil Cells (LDC–DACs)

A typical ***laser-driven dynamic compression diamond anvil cell (LDC–DAC) experiment is illustrated in Figure 2A–D***. LDC–DAC systems include a pulsed laser system ((i), not shown), a focused laser beam (ii), a material sample to be compressed (iii), at least one diamond anvil (iv), a chamber gasket (v), and an optional laser target (xvii) placed at the laser focus. Diamond is commonly used for the transparent anvils (iv) in LDC–DAC experiments due to its high shock impedance, wide transmission bandwidth, and dielectric constant [22], although other materials, such as sapphire (Al_2O_3) and quartz (SiO_2), have been utilised [32,46–48].

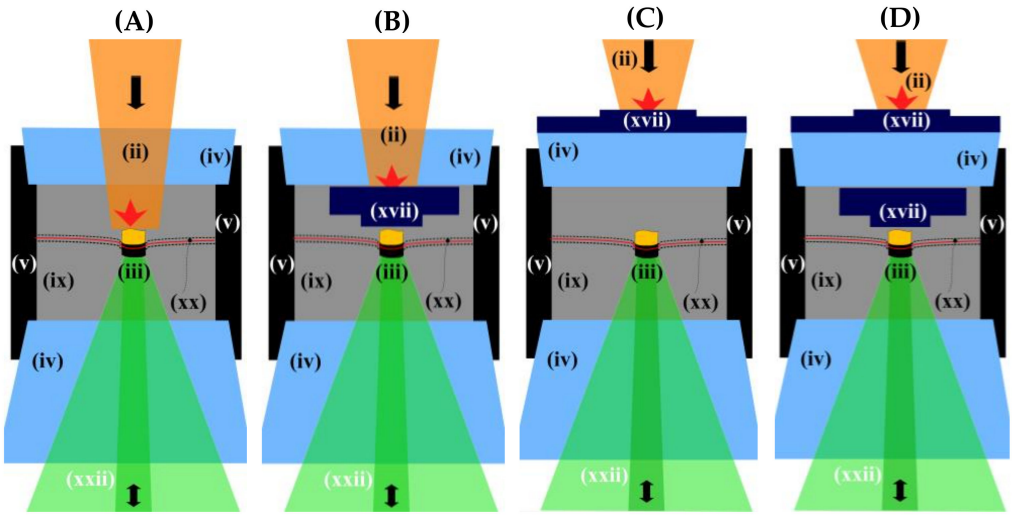

Figure 2. Illustrations of laser-driven dynamic compression diamond anvil cell (LDC–DAC) experiments. (**A**) The sample of interest is the target, (**B**) a separate target inside the anvil, (**C**) a target outside the anvil, and (**D**), a target outside and driver inside the anvil. Please see article text for component descriptions.

In some experimental setups, the sample itself is the laser target, as displayed in Figure 2A [22,30,49]. In most configurations, however, a target comes before the sample to be compressed (See Figure 2B–D). The laser target's purpose is to absorb the laser light before it arrives at the sample; this target can be placed in several locations, such as at the inside surface of the incident anvil (Figure 2B) [24,25,50–53], or on the exterior surface of the same anvil (Figure 2C) [54–56]—or on both surfaces of the incident anvil (Figure 2D) [29,46,47,57–61]. Note that in the references for Figure 2C, the examples

provided are not strictly L-DACs but are arranged similarly to that of an L–DAC (with a fully enclosed pressurised cell). Many variations on these configurations have been attempted in the past [46,62–64].

In LDC–DACs, the laser system typically includes a high-peak-power laser, with pulse widths ranging from nanoseconds down to picoseconds. As each focused laser pulse arrives, a portion of the target is ablated, a plasma plume emerges, and a shock- or pressure-wave (xx) results which passes through the sample (iii); these pressure waves or shockwaves momentarily act as a "second stage" DAC to locally compress the sample to higher pressures, while maintaining the DAC's background pre-compression pressure [20]. Often rarefaction waves follow the shock- or pressure-waves [65], and all of these waves reflect (somewhat) at interfaces between materials, e.g., where the target contacts the sample [61]. These waves can subsequently interfere with each other, which often degrades (or enhances) the compression [58].

Pressure waves are broadly defined as a disturbance that propagates through a medium at sonic velocities [66–68]. Shockwaves typically propagate faster than the speed of sound and there is an abrupt change in pressure as the wave arrives (approaching that of a step function) [68]. In LDC–DAC systems, pressure waves and shockwaves are generated from a combination of the instant (thermal) pressure induced by the expanding plasma and momentum transferred to the target as material is ablated away [57]. As the applied driving energy increases, i.e., the intensity of the laser, the velocity and amplitude of the wave typically increases proportionally [60,66,68,69].

Using nanosecond and shorter laser pulse widths, researchers can drive samples without a significant temperature rise during compression. This is beneficial for several reasons: first, it permits materials to be compressed in an isentropic manner, so that their density/structure can be more easily determined [31]. Second, large-scale diffusion is delayed or prevented—which otherwise leads to contamination—as is known to occur during LH–DAC experiments [70]. Third, samples may be retained in a solid phase rather than melting immediately, so that potential new solid phases can be identified [31]. Fourth, thermal stresses on the anvil's materials are often reduced, extending the pressure range of the devices [25]. And finally, short-pulse widths provide access to extreme pressures, but at low-to-moderate temperature ranges, which are not otherwise readily accessible (refer to the lower portion of the red boxed region in Figure 3) [22,24,32,47,49]. For instance, samples possessing cryogenic boiling points, such as H, He, Ar, etc. are much easier to compress from cooled samples when laser heating does not occur [71].

Note that the *low-temperature*, high-pressure region (<500 K, 100–600 GPa) is also similar to conditions anticipated within many ice moons or gas giant planets [22], (for reference, estimated P–T conditions within several planetary bodies are provided in Figure 3). Many investigators attempting to clarify the internal structure of planetary bodies are conducting LDC–DAC experiments. For example Kimura et al. studied many of the primary constituents in our solar system, including the low-Z compounds: H_2, He, H_2O, NH_3, and CH_4, and determined their EOS to better model planetary dynamics [22]. Another study by Eggert et al. attained Hugoniot data of fluid He at moderate temperatures and within the hundred GPa regime using LDC–DAC [47]. From this, Eggert et al. measured material properties that had previously been predicted by Path-Integral Monte Carlo (PIMC) and Activity Expansion (ACTEX) calculations [47]. Similarly, Rygg et al. measured the crystal structures of C, MgO, Fe, Cu, Zr, Sn, Ta, and Pb samples at up to 900 GPa and close to 300 K [49].

LDC–DAC experimentation has also been used to examine materials within high-pressure, high-temperature (HPHT) regimes that are difficult to access otherwise (>5000 K, >250 GPa) [22]. For instance, hydrogen's phase diagram was explored at conditions at a depth of ~7000 km within Jupiter's atmosphere (~5000 K and ~50 GPa) [21,72], and researchers were able to investigate the potential for metallisation of water at up to ≈19,000 K and 250 GPa with 4 ns laser pulses [30]. Similarly, Coppari et al. obtained phase transition data and the EOS of magnesium oxide over the range of 4000–9000 K and 600–900 GPa util-

ising ≈4.5 ns laser pulses [30]. And finally, Loubeyre et al. extended the known properties of hydrogen and deuterium over the range of 297–40,900 K and 0.3–175 GPa using 1-ns laser pulses [28]. In all these cases, high fluences and extended pulse widths (≥1 ns) were employed to ensure both strong shock loading and heating of the samples [26].

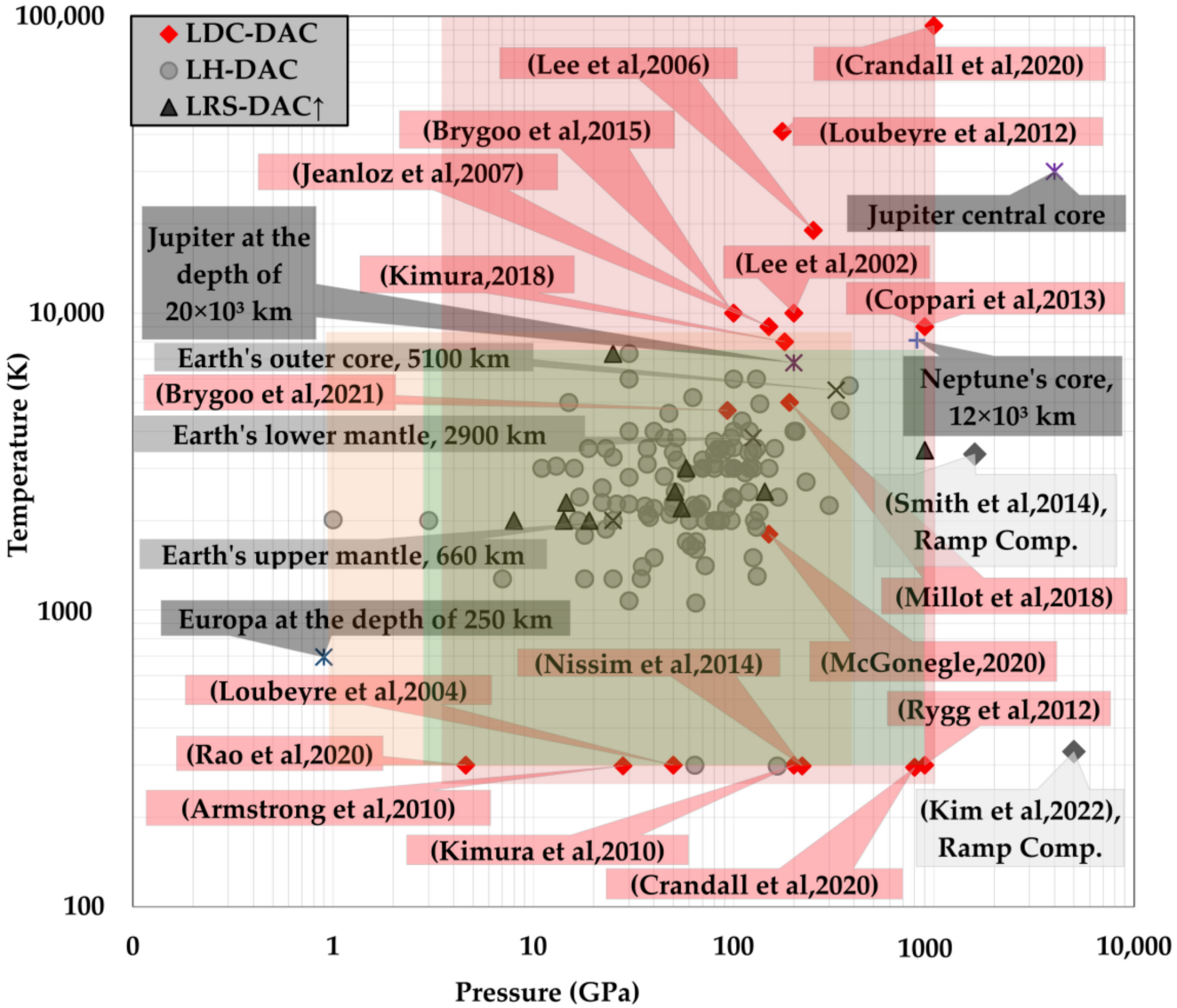

Figure 3. P–T diagram of L–DAC experimentation, showing region investigated by LDC–DAC systems (Red) [21,28,30,57–60,73,74], LH–DAC systems (Orange) [8,20,75–190], and LRS–DAC systems (Green) [191–198]. For reference, P–T markers are also provided for several geophysical locations, including the P–T at a depth of 250 km of Europa's oceans [199], 60–5100 km underneath the Earth's surface [60,105,161], 12 × 10^3 km-deep in Neptune's core [200], (20 to 71.5) × 10^3 km-deep in Jupiter's core [201,202] and two LDC experiments with ramp -compression [37,38].

A primary advantage of the LDC–DAC experimental mode is the ability to control initial-, peak-, and final-conditions (ρ-P-T) of the sample material. For example, initial densities of a sample are controlled via (isothermal) compression within a DAC prior to delivering a laser shock, while the maximum (peak) compression is obtained through the laser fluence, pulse width, pulse shape, and target/sample geometries. By conducting the experiment within a DAC, the material arrives at a final, elevated pressure, making it possible to preserve metastable states that would otherwise deteriorate at lower pressures (which sometimes happens when using LDC alone) [22].

Nevertheless, LDC–DACs do have some limitations, and as shown in Figure 1B, comprise only a minor fraction of all L–DAC publications. This may in part be due to the complexity of the experiments and/or lack of access to the necessary high-energy laser sources [19]. In addition, there is a limited selection of material characterisation probes that can be used during LDC–DAC experiments, where real-time, ultrafast characterisation is required. One important complication is the requirement for custom anvil shapes—often thick on the opposing (diagnostic) anvil (iv), and thinned on the incident (drive beam) anvil (iv)—and specialty shapes are often needed along the laser beam path [25]. The opposing anvil material must also be designed to have high impedance matching with the sample [31].

Of course, a significant limitation is the strength of the anvil materials in their required geometries. Diamond is the most commonly-used anvil material, yet it is often thinned to <400 micron thicknesses on the incident anvil [57]. Diamond anvils are subject to failure during compression experiments, which raises the experimental cost, and requires significant effort to reset the LDC–DAC system for subsequent runs. Although sapphire has lower compressive strength (~2 GPa static, ~21 GPa dynamic) than diamond (~35 static, ~98 GPa dynamic), it has also been used as an anvil material during LDC–DAC experiments [32,46,203–205]. Similarly, quartz has also been used as an anvil or window (~1 GPa static, ~9 GPa dynamic) [206,207]. Further research is required to maximise the peak pressures attained during shock loading and minimise the cost/effort of LDC–DAC experimental runs [49].

4. LDC–DACs: Physical Processes, Historical Development, and Key Experiments

Figure 3 offers an overview of the maximum pressures/temperatures achieved by researchers during LDC–DAC experiments (red-shaded region), in comparison to those employed during LH–DAC experiments (orange-shaded region) and LRS–DAC experiments (green-shaded region). For reference, various pressures/temperatures estimated for geophysical and astrophysical sources are also displayed (cross-symbols). Note that for the ***laser heated-diamond anvil cell* configuration**, static pressures of up to ~380 GPa have been achieved using *single-stage* DACs, as well as laser-induced (constant) temperatures of up to ~7500 K [80,161]. Even greater *static* pressures can be attained using multi-stage DAC's, as discussed in part I of this review. For comparison, the LDC–DAC configuration has attained dynamic pressures approaching 1 TPa, and temperatures of up to 93,000 K [30]—as shown at the red region's upper and right hand sides. Of course, the reader should be cautioned about comparing static and dynamic pressure values, as their compression mechanisms are different. Even greater dynamic pressures have been proposed as theoretically feasible (to 100 TPa) [57]. With the exception of a recent experiment with rhenium nitride [208], *LRS–DAC* experiments, shown within the green region, present a similar range of pressures and temperatures to the LH–DAC mode, as similar laser sources are employed, although the majority of LRS–DAC studies have been conducted at temperatures below 3000 K.

A typical LDC–DAC system is illustrated in Figure 4, with primary laser source (i), where focused laser beam(s) (ii) illuminate a pressurised sample (iii) through transparent anvils (iv), within a gasket chamber (v). Additional common components of an LDC–DAC system include: diamond seats (vi), a mechanism for driving the diamond anvils together (vii), laser beam delivery optics (viii), pressurisation media (ix), optical pyrometers to measure sample temperatures (x), an optical system with spectrometer for pressure measurements (e.g., via ruby fluorescence [209]) (xi), and microscopes for general sample observation and process controls (xii) [1,6]. ***LDC–DAC systems typically*** include components beyond that of an LH–DAC set-up, such as a target (xxvii) at the pulsed laser focus and diagnostic tools, e.g., a ***velocity interferometer system for any reflector (VISAR)*** (xxi).

Most prior *LDC* experiments have been conducted using pulse widths in the order of 1–10 nanoseconds (See Tables 1 and 2), but a few have been carried out with short-pulsed lasers (below 350 ps) [24]. Note that the target may consist of the sample itself [25,50] or a

separate target, sometimes called a "driver plate," or "flyer plate" (xvii) [19,20,57]. Several different target materials have been reported in the literature, including gold, titanium, aluminium, and quartz [46,47,50,58,74]. Often the laser pulse shape (in the time domain) is controlled to give the material time to respond. Sometimes a pulse train of two or more shaped laser pulses are ramped up to a maximum fluence over ~45–110 ns [32], so that energy accumulates at the front of the shockwave; this provides a higher final peak compression and is known as ***ramp pulse compression (RPC)*** [30,31]. Many *LDC–DAC* experiments have used RPC to achieve peak laser-induced pressures of up to 900 GPa (see right side of red region in Figure 3) [49].

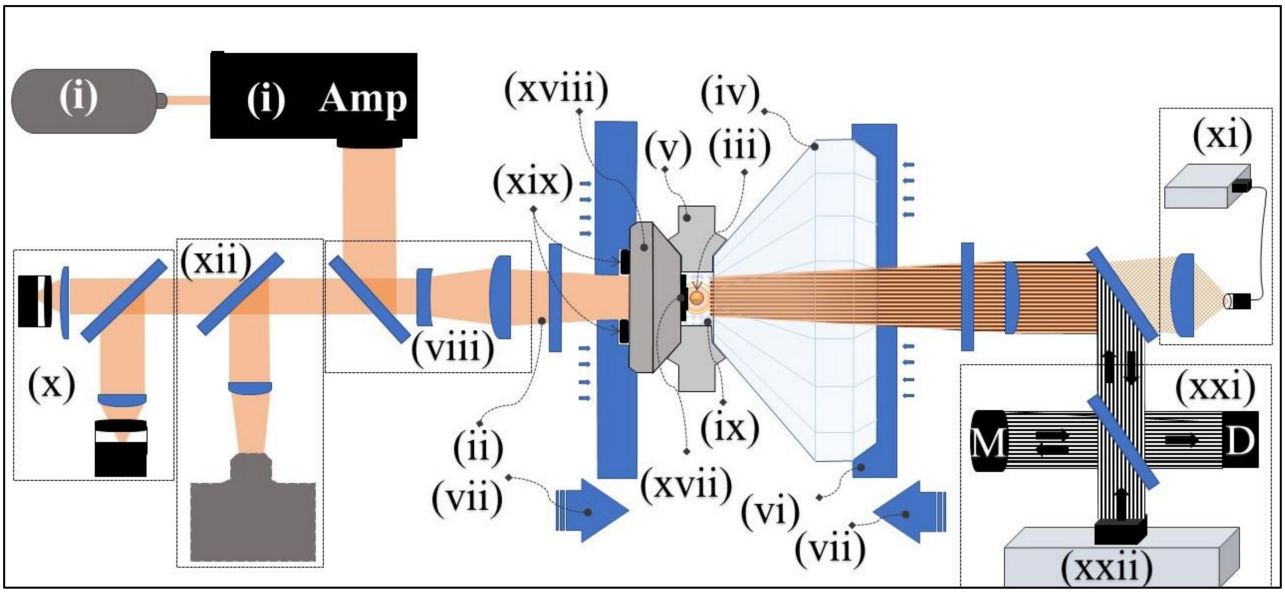

Figure 4. Typical arrangement of laser-driven dynamic compression diamond anvil cells (LDC–DAC), systems for scientific/engineering experiments. The various components of these systems are described in the text.

In some experiments, multiple *shocks* have been used to advantage by launching two or more sequential shocks into a sample [46,47], which can provide access to higher material densities [48,210]. Sometimes this is called the "double-shock" technique or "re-shock" technique [48,210,211]. For example, Crandall et al. studied the "re-shock states" of carbon dioxide at pressures between 71–189 GPa using dual-, back-to-back, 1 ns pulses, while maintaining nearly isothermal conditions of ~300 K [46].

When very "cold" shockwaves are desired, ultra-short laser pulses (<100 ps) are also often employed [19,24,58]; this limits the average power delivered and helps to prevent sample heating. When samples are repetitively shocked using such ultra-short laser pulses, this has been dubbed "*nano-shocking*;" in this case, the pulses are short enough that even microscopic samples can be shocked repetitively over a timescale of <<100 nanoseconds with minimal heating [212]. This opens the door to novel thermodynamic pathways, where samples can be compressed to much higher densities without necessarily increasing their internal energies [46].

Table 1. (H, He)-Based, Low-Z Fluids studied/modified in selected LDC–DAC works.

Modified Material and/or Property	Starting Material	Static Press. [GPa]	Shock Press. [GPa]	Laser Type [nm/μm]	Laser Parameters: Powers/Energies [W/J], Spots [μm], Ind. Temps [K]	Refs
Ionised H_2O, EOS	H_2O	≈1	≈50–300	Nd:YAG, 1.06 μm	Pulsed, 4 ns, ≤500 J, ≈5×10^{13} W/cm^2, ≈300 μm	[25]
H_2O, Sound velocity, Hugoniot Curves, EOS	H_2O	a: 0.57	a: 288–342	a: Nd:YLF, 351 nm	a: Pulsed, 3 ns, 800–1500 J, 650 μm	a: [29]
		b: ≈1–5	b: 150	b: Nd:YAG, 532 nm	b: Pulsed, ≈10–20 ns, 1–10 kJ, ≈200–500 μm, 6–9 × 103 K	b: [57]
		c: 0.1–0.6	c: 283	c: Nd-glass laser	c: Pulsed, 1.5 ns, 1 kJ, Max 4 × 1014 W/cm^2, 500 μm	c: [51]
		d: ≈1	d: ≈200	d: Nd:glass laser	d: Seven Pulsed beams, 4 ns, 1013–1014 W/cm^2, 104 K	d: [50]
		e: ≈1	e: 250	e: Nd:glass laser	e: Pulsed,1–4 ns, ≈300 μm, 1014 W/cm^2, 19 × 103 K	e: [26]
		f: 1.33	f: 200	f: N/A	f: 800–1000 μm, 300 K	f: [22]
H_2, Hugoniot curves	H_2	0.7, 1.2	≈20 −50	Nd:YAG, 1.06 μm	Pulsed, 1.2 ns, 10^{14} W/cm^2, 400 μm, 300 K	[21]
H_2, D_2, EOS, Hugoniot Curves	a: H_2 b: D_2	0.16–1.6	a: 104 b: 175	Nd:glass laser, 351 nm	a: Pulsed, 1 ns, 6 kJ, 800 μm, ≈27.7×10^3 K b: Pulsed, 1 ns, 6 kJ, 800 μm, ≈40.9×10^3 K	[28]
He, Hugoniot Curves	He	0.11–1.25	117	Nd:glass laser, 351 nm	Pulsed, 10.6 ns, 3 kJ, 800 μm	[47]
He EOS, Hugoniot Curves,	He	1.25	200	Nd:glass laser, 351 nm	Pulsed, 1 ns	[52]
H_2–He, EOS	H_2–He	4	93	Nd: YAG laser, 351 nm	4–6 kJ, 1 ns, 4700 K	[60]
He, H_2, EOS	He, H_2	5	100	Nd:glass laser, 351 nm	Pulsed, ≈5–25 ns, 1–6 kJ, 800 μm, 10×10^3 K	[59]

Table 2. High-Z materials/minerals modified in selected LDC–DAC studies.

Modified Material and/or Property	Starting Material	Static Press. [GPa]	Shock Press. [GPa]	Laser Type [nm/μm]	Laser Parameters: Powers/Energies [W/J], Spots [μm], Ind. Temps [K]	Refs
Ar, Shocked States	Ar	≈7.8	28	A Pulsed laser ≈ 300 ps, 800 nm center λ, 25 nm bandwidth pulse	≈100–300 μJ, 20 μm to 50 μm, 298 K	[24]
C_6H_6, Phase transitions, Structures	C_6H_6	N/A	4.6	Nd: YAG laser, 1064 nm	a: 0.7 J, 9–108 ns b: 0.1–1.3 J, 52 ns ≈2 J/7 ns, 1800 μm, 300 K	[32]
CO_2, EOS	CO_2	1.16	1000	Nd:glass laser, 351 nm	8×10^{14} W/cm^2, 93×10^3 K	[27]
CO_2, Sound velocity	CO_2	0.36–1.16	800	Nd:glass laser, 351 nm	480 J/beam = 5670 J, 1.2–10 $\times$ 10^{14} W/cm^2, 1 ns, 865 μm, 298 K	[46]
SiO_2, EOS	SiO_2	5	100	Nd:glass laser, 351 nm	Pulsed, ≈5–25 ns, 1–6 kJ, 800 μm, 10^4 K	[59]
Al, Hugoniot Curves	Al	≈50	≈200	Pulsed laser	Pulsed, 1–2 ns, 10^{14} W/cm^2, ≈500 μm	[58]
CsCl-type MgO, EOS, Structure	NaCl-type MgO	≈60	600 to 900	Nd:glass laser, 351 nm	≈4.5 ns, up to 37 kJ UV, ≈300 μm, 4–9 $\times$ 10^3 K	[30]
Fe, Sn, Ta, Pb, and MgO, Structure	Fe, Sn, Ta, Pb, and MgO	N/A	900	Temporally shaped laser pulse	10^{14} W/cm^2, 800 μm, 300 K	[49]
Al, Ta, and W, Sound velocity Hugoniot Curves	Al, Ta, and W	N/A	220	Pulsed laser	Pulsed, 1–2 ns, 10^{14} W/cm^2, ≈500 μm, 298 K	[73]

4.1. LDC–DACs: Physical Processes

The progression of a pressure wave or shockwave from a target through a sample is illustrated in Figure 5, with a dotted red line (moving in the direction of the lower white arrow). In many experiments, the impinging beam (purple) is chosen to have a large-diameter, *top-hat spatial beam profile* (dotted curve), that induces a broad, ablated plasma plume (red dome); this, in turn, drives the target (silver plate) over an extended area. The material sample is shown in black below the target. The example shown is of the LDC–DAC type illustrated in Figure 2B, with an internal target adjacent to the sample.

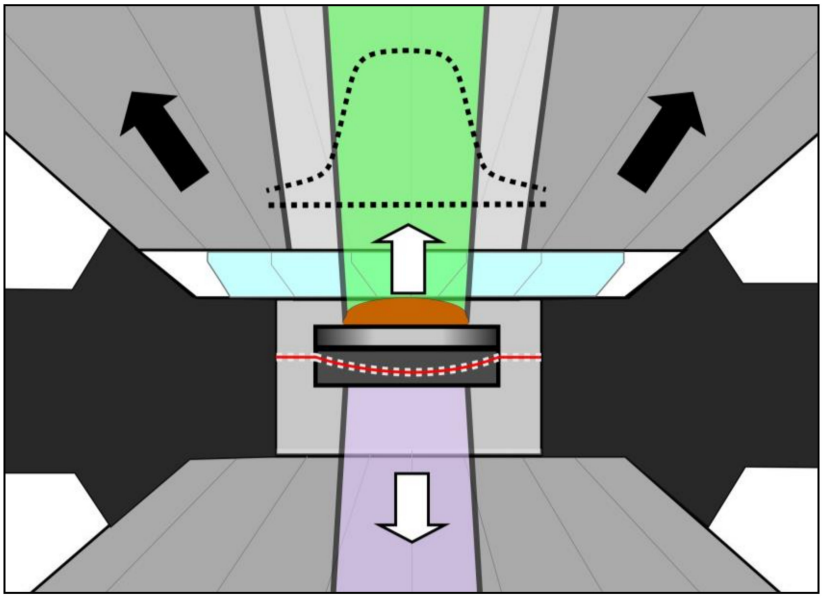

Figure 5. Schematic of dynamic compression in an LDC–DAC with internal target (See Figure 2B), showing an impinging laser beam (green) on a target (graded plate). The target is partially ablated, resulting in a plasma plume (orange dome), with a shock (or impulse) passing through the sample (hashed lines). Heat transfer occurs initially through radiation from the plasma (black arrows). A Reflected wave eventually travels back toward the laser source (upward white arrow).

Now, during LDC–DAC experiments, single-pulse intensities on the order of 1–100 petawatts/cm^2 or greater are typical [46,58,73]. When an incident laser pulse is absorbed, the induced high-temperature plasma expands rapidly from the target into the surrounding pressure media on picosecond to nanosecond timescales [24,32,57]. The magnitude and rate at which this energy is applied (given the laser pulse-width and fluence) determines whether this plasma expansion will induce a pressure wave or shockwave at the target. At petawatt/cm^2 energies, this often produces very rapidly expanding shock waves. In this case, using *point-geometry, strong explosion theory*, the generalised velocity of a shockwave expanding into a fluid, v_{sw}, takes on the form:

$$v_{sw} = \alpha \left(\frac{E_{lp}}{\beta \cdot \rho_i} \right)^n t^{-m}, \tag{1}$$

Here, E_{lp} is the laser pulse energy absorbed, ρ_i is the initial (rest-state) density of the gas, and β is a constant that depends on the gas' adiabatic constant. For a spherical expansion, α, n and m, are derived to be 2/5, 1/5, and $-3/5$, respectively, i.e., [213]:

$$v_{sw} = \frac{2}{5} \left(\frac{E_{lp}}{\beta \cdot \rho_i} \right)^{1/5} t^{-3/5}, \tag{2}$$

Non-spherical, but related spheroidal geometries, can be approximated using analogous equations to (1), but with altered constants α, n and m specific to vector directions. Equations (1) and (2) are valid for large shock velocities above Mach 2 [213]. Note that as the shock velocity is proportional to E_{lp}^{n}, where $n << 1$, the shock velocity increases *slowly* with rising pulse energies. In addition, as time increases, v_{sw} drops from its peak value by t^{-m}; this leads to order-of-magnitude decreases in shock velocities over timescales of 10 ns or more. Thus, for targets and samples other than very thin films, the change in shock velocity over time must be considered when designing experiments.

Provided sufficient travel time, both on-axis back rarefaction and side rarefaction waves can catch-up with, and interfere with, the primary shock wave. To prevent this (e.g., for the configurations of Figure 2B,C), the transit time must be kept short, so the thickness of the target (or anvil), X_t, must be no more than the "catch-up" distance, ΔX, of the back rarefaction wave [58], i.e.,:

$$X_t < \Delta X = \left(v_{sw}^2 \Big/ v_{mc} \right) \tau \tag{3}$$

Here v_{sw} is the shock wave velocity, v_{mc} is the velocity at which the sample material responds and moves, and τ is the laser pulse width. In many experiments, authors have tended to use long τ times, to give the longest possible catch-up distances.

To minimise shock reflections and consequent re-shocking of the sample (upward white arrow in Figure 5), materials at each interface are chosen to have comparable *shock impedances* [28,46,47,214,215]. The thinned diamond anvils are sometimes backed by tungsten carbide anvils for this purpose, as shown in Figure 4 (xvii) [25,29]. The transparent anvil material must also be selected carefully, as certain optical materials become opaque during/after a shockwave; sapphire anvils have been used to avoid this problem [216].

The *rate* at which the laser energy is applied also determines how much heating the sample ultimately receives *during compression*. On the lower end of the pulse-width range (<<100 picoseconds), there is little time for *diffusive* heat/mass transport to occur away from the immediate focal region. In most cases, radiation is (initially) the primary mode of heat transport (represented by the black arrows in Figure 5), with diffusive and advective transport occurring much later [21]. Consequently, while the temperature rises in the expanding plasma at rates of 10^{11} K/s or greater [217], the remainder of the sample (and any surrounding pressure media) initially remain near the DAC's background temperature. This is what allows for adiabatic and isentropic material compression, where work is done to the sample material before significant diffusive heating occurs [20,57,97,218].

In fact, it can be shown that, a shock or pressure wave ($\geq$Mach 1) can initially outpace the diffusive heat propagation wave initiated at a target [65,219]. Defining the heat wave velocity as v_{hw}, Eliezer et al. arrives at the relation:

$$v_{hw} = \frac{dx_{hw}}{dt} \propto t^{-1/(n+2)} \tag{4}$$

Here, x_{hw} is the position of the propagating heat wave from its origination point (laser focus), t is the time from the initiation of the laser pulse (which varies between $0 \leq t \leq \tau$), and n is an exponent describing any non-linearity of the thermal diffusivity, α_T, with temperature (when $n = 0$, the thermal diffusivity is a constant). For hot electrons in a plasma [64], it can be shown that $n \approx \frac{5}{2}$. In this case, Equation (4) simply becomes:

$$v_{hw} \propto t^{-2/9}. \tag{5}$$

In Figure 6, the magnitudes of Equations (2) and (5) are compared over time, all other factors being normalised. Note that initially, the shockwave (blue-dashed curve) outpaces the heat wave (orange-dotted curve), allowing isentropic compression to occur within the hashed region. Sometimes this allows the heat-wave to enter the rarefraction wave, as it lags behind the shockwave [219]. Over longer time-periods, the shock loses speed, and the heat-wave eventually overtakes it. One notable example in the literature is the work of

Babuel-Peyrissac et al., who modelled how v_{hw} initially lagged behind v_{sw} and generated a *separation region* where material was shocked but with limited heating. The assumed laser fluence was 10^{15} W/cm^2, incident on a deuterium sample, and the time to separation between the two heat/shockwaves was estimated to be only 48 ps—much shorter than the length of the incident laser pulse [219]. In Figure 6, it is assumed that the heat and shockwaves are separated throughout the observed timescale. Hence, careful experimental design is necessary to obtain isentropic processing—which must account for the timing of each wave and the thicknesses of targets and samples.

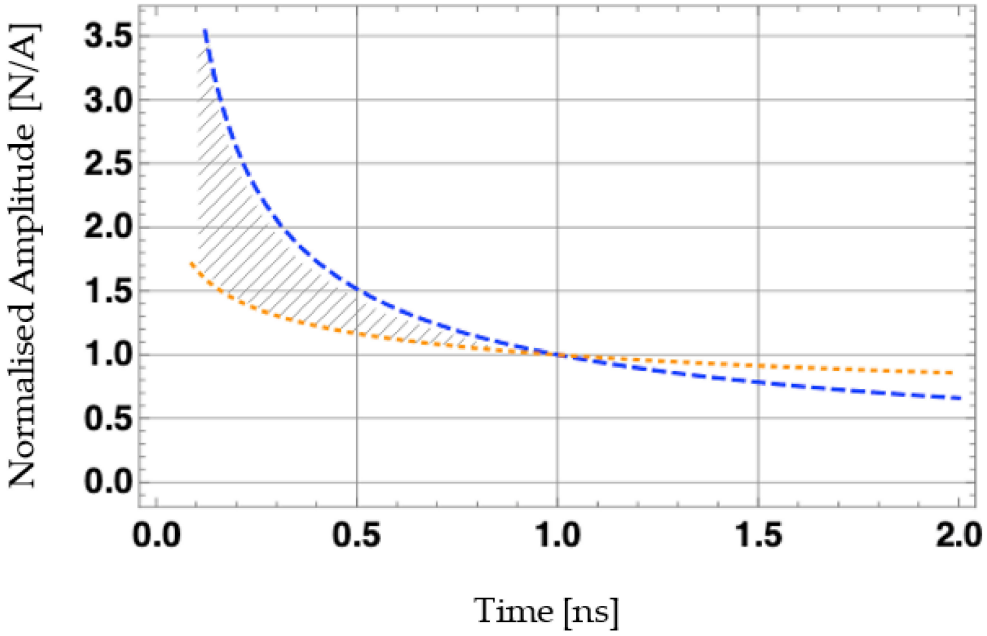

Figure 6. Comparison of the shockwave and heatwave velocities, v_{sw} and v_{hw}, for short time durations to a pulse width of 2.0 nanoseconds. Note that the shockwave (blue-dashed curve) initially outpaces the heatwave (orange-dotted curve), allowing for isentropic processing within the hashed region.

Now, provided that either (1) a single-laser pulse is used, or (2) a low pulse-repetition-rate (PRR) beam is employed, the *average thermal energy* transferred *into a sample* can actually be quite low, even when extremely high peak intensities per pulse are employed (e.g., >10^{15} W/cm^2·pulse)—provided ultra-short laser pulses are employed (τ << 100 ps). So, unlike the continuous-wave (cw) laser heating used in many LH–DAC experiments, LDC–DAC experiments may be designed to not necessarily *heat* samples during compression.

Determining shock and the material compression velocities is important to be able to estimate the density, volume, and energy of the sample material $\rho(t)$, $V(t)$, $E(t)$ throughout the laser dynamic compression process. The *Rankine-Hugoniot* relations express the conservation of mass, momentum, and energy for a sample transitioning from an (initially) unshocked state (i) to a (final) shocked state (f). Defining the velocity at which the sample material compresses, v_{mc}, one obtains:

$$P_f \Big/ \rho_i = (v_{sw} \cdot v_{mc}) \tag{6}$$

$$V_f \Big/ V_i = (v_{sw} - v_{mc})/v_{sw} \tag{7}$$

$$\left(E_f - E_i\right) = P_f \cdot \left(V_i - V_f\right)/2 \tag{8}$$

A sequence of shock compressions that conserve mass, momentum, and energy (as above) is known as a *Hugoniot curve* [58]. A rapid sequence of laser pulses can drive a sample material to follow such a Hugoniot curve [220]. The term *Hugoniot* has been

utilised in the literature to refer to material responses in which the resulting material states differ from those obtained through processes where equilibrium conditions are attained [221]. Hugoniot material responses are of interest due to applications where non-equilibrium processes occur such as in meteorite impacts, explosive volcanology, or novel manufacturing processes [222].

In order to better determine Hugoniot curves, three laser-based characterisation techniques may be employed to measure v_{sw} and v_{mc} experimentally: (1) *velocity interferometer systems for any reflector* (VISAR), (2) *laser Doppler velocimetry (LDV)*, and (3) *optically recording velocity interferometer systems (ORVIS)* [25,57,223,224]. These techniques are also more generally applied in dynamic compression experiments, e.g., gas-gun tests, and can be used individually or in combination. VISAR measures the free-surface position/velocity of a shocked sample by observing the reflected beam with an interferometer, while LDV measures the Doppler shift of a laser beam reflected off the same free-surface. ORVIS measures the free-surface velocity by recording parallel fringes generated from an interfering laser beam using high-speed and streak cameras.

Knowing v_{sw} and v_{mc} from the characterisation methods described above, the actual *rates* of sample material compression can be estimated. As shown in Figure 7, LDC–DAC methods complement static (DAC) and *dynamic* (D-DAC) methods because each operates on different timescales. Static DACs, on the left-hand side of the scale, are compressed/released relatively gradually (typically << 10 GPa/s) [225]. D-DACs, on the other hand, controllably compress or release samples at rates of 10^{1}–10^{5} GPa/s, depending on their configuration [225–228]. Stepper-motor-driven dynamic DACS (sometimes known as S-DACs) are often the slowest of these with rates <10^{2} GPa/s, followed by gas-driven membrane DACs (i.e., M-DACs) with rates of 10^{4} GPa/s or less [227,229], while piezoelectric DACs (P-DACs) and combination stepper-motor/piezoelectric DACs (S/P-DACs) are operated at compression rates of up to 10^{4}–10^{5} GPa/s [226]. In contrast, LDC–DAC systems allow compression/release rates four to seven orders of magnitude greater than all dynamic DACs (i.e., 10^{9}–10^{12} GPa/s); this enables access to novel material states and potential new synthesis routes. For comparison (see the far right-hand side of Figure 7), Caudle et al. recorded one of the highest compression rates ever, >10^{15} GPa/s, during an HP–MB–LDC experiment—but without pre-compression within a diamond anvil cell [230].

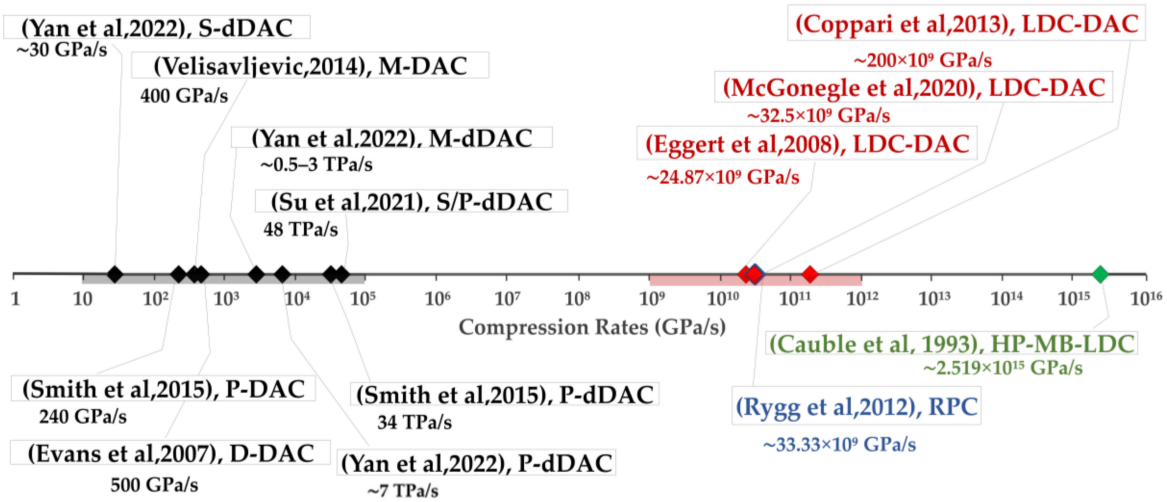

Figure 7. Compression rate of several DAC methods including; Stepper motor- dynamic (S-dDAC) [227], a piezoelectric driven (P-DAC) [228], a standard gas-Membrane (M-DAC) [229], dynamic (D-DAC) [225], gas Membranes dynamic (M-dDAC) [227], a Piezoelectric driven step compression dynamic (P-dDAC) [227,228], Static and dynamic (S/P-dDAC) [226] in comparison to LDC-DAC (Red) [30,31,47], ramped pulse compression (RPC) (Blue) [49], and HP–MB–LDC (Green) [230].

From Equations (6) and (7), one can see that the shockwave velocity (v_{sw}) is a crucial parameter in the Rankine–Hugoniot relations, and it is used to derive final state data (e.g., ρ, P, T) [24,26,32,49]. v_{sw} can be measured using a VISAR or ORVIS system (as described above) [59], or through measurements of the Raman intensity emitted from a laser-illuminated sample over time. In this latter case, one can estimate the shock velocity from the slope, σ, of the shocked Raman intensity (normalised to its unshocked intensity) versus time. The product of σ times the sample target thickness, d, provides the shock velocity, i.e., [32,231].

$$v_{sw} = (\sigma \cdot d) \tag{9}$$

While a pressure wave travels at the speed of sound in a medium, v_{pw}, a true shockwave travels at $v_{sw} > v_{pw}$. By using line-imaging VISAR, these two velocities (v_{sw} and v_{pw}) can be related to the material compression velocity (v_{mc}) through the simple relation [29]:

$$v_{pw} = v_{sw}\sqrt{\left(\frac{v_{sw} - v_{mc}}{v_{sw}}\right) + tan^2\theta} \tag{10}$$

Here, θ is the angle measured between the retarded wave front and the edge of the shockwave front. So, by measuring shock and compression velocities, one can readily derive local sound speeds in a solid (v_{pw}).

Knowing the actual sound (acoustic) velocity vs. density, pressure, and temperature is critical in many areas of geo- and planetary-physics, because modelling the interior structures of these bodies (and seismic events on Earth) often relies on acoustical timing measurements [73]. Equation (10) is also useful in deriving EOS variables (e.g., ρ, P, T, E) from shock velocity measurements [73,232,233]—and in simulating diffusion and density-driven advection on both small- and large-length scales [65,73]. The Gibbs free energy of phase transitions, ΔG_{ph}, can also be derived from acoustic velocity measurements [29].

Now, as shockwaves may generate a significant number of defects in crystalline materials [234], it is not always desirable to *shock* some samples during LDC–DAC experiments. Excessive shock intensities may convert much of the shock's energy to entropy and heat, rather than sample compression [20,235]. For these reasons, a sequence of laser pulses is often used, similar to RPC. This generates a gradual impulse on the order of 10–100 ns, which is sometimes known as shockless-compression [20]. Shockless compression makes it possible to minimise shock heating, while compressing samples to higher pressures [49].

4.2. LDC–DAC: Historical Development and Key Experiments

The inspiration for laser dynamic compression in a DAC came from P. W. Bridgman in 1956 who predicted that static pre-compression would be combined with shock compression [236]. However, to our knowledge the first implementation of an *LDC–DAC* experiment was in 2001, when Moon et al. at Lawrence Livermore National Laboratory introduced a new LDC–DAC design, in which thin diamond plates backed by tungsten carbide replaced the traditional diamond anvils; this allowed for pre-compression of H_2O samples to 1 GPa, followed by laser driven compression to ≈50–300 GPa [25]. From this they estimated the Hugoniot curve for water in a P–T region not previously accessed. Their LDC–DAC design, similar to that of Figure 2B, used a separate target inside the anvil to prevent the laser-generated shock from spreading (and losing intensity) before passing through the sample; this approach greatly influenced future implementations of LDC–DACs.

In 2007, this same group extended their research to temperatures in the range of 6000–9000 K, using a configuration akin to Figure 2D [57]. They found that water forms a metallic-like phase within shock fronts at 100–150 GPa. Rather than transmitting an incident beam (from a ***VISAR***), the compressed water reflected the laser beam, and the velocity of the shock front could be determined. The VISAR system was arranged similarly to the basic interferometer of Figure 4 (xxii). In conjunction with this work, Jeanloz et al. estimated that the LDC–DAC method could theoretically be extended to peak dynamic pressures in the 10–100 TPa range [57]. Although this prediction has yet to be realised, peak

pressures by laser dynamic compression (LDC) are now approaching the predicted lower bound of this range (10 TPa) [27]. These two developments are shown on the left-hand side of the timeline in Figure 8.

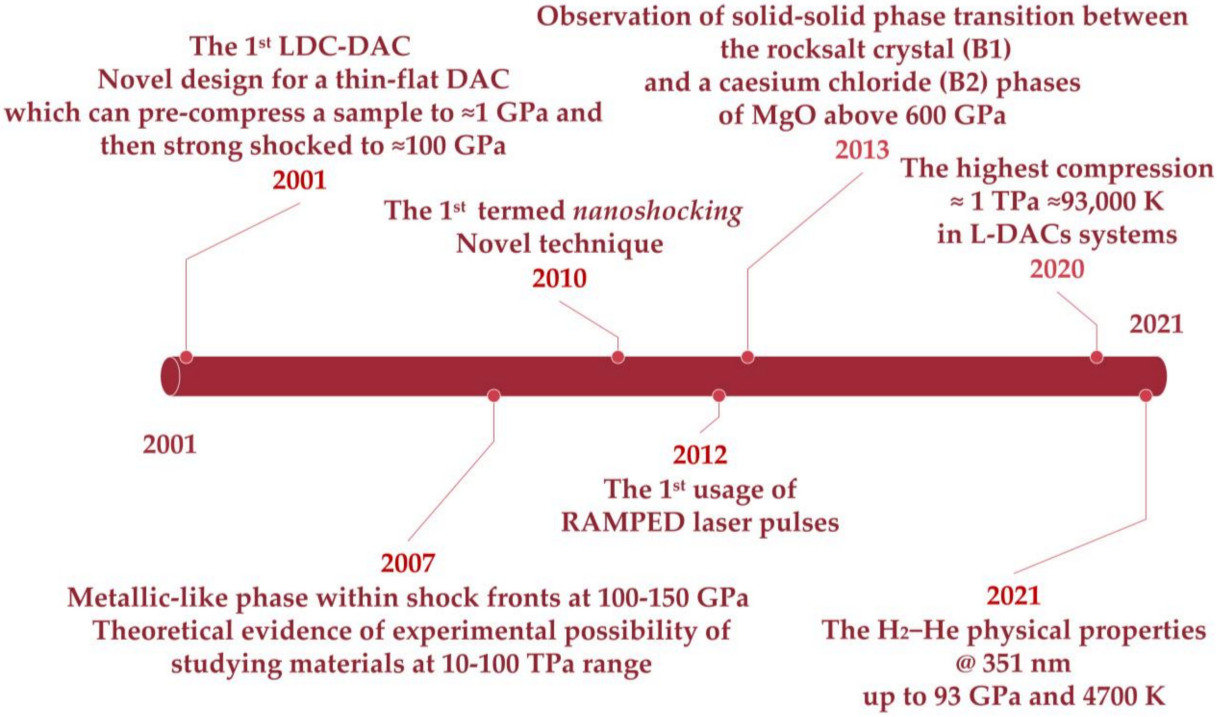

Figure 8. Chronology of key laser-generated shock compression diamond anvil cell (LDC–DAC) developments and events.

The concept of ***Nanoshocking***, was first introduced in 2010 by Armstrong et al. at Lawrence Livermore National Laboratory, using the configuration of Figure 2B, with a~1 μm thick aluminium target on the inside surface of the (incident) diamond anvil [24]. In this case, a series of ultra-short sub-10 *picosecond*, 100–300 μJ pulses were used to generate "nano-shockwaves" at the aluminium target—which subsequently passed through argon/nitromethane samples within the DAC. Meanwhile, a train of lower-power probe pulses were directed onto the sample through the DAC backside anvil, and the reflected (and wave-front distorted) probe pulses were analysed by means of a spectrometer and high-speed imager. Using such short timescales allowed for near-adiabatic compression of the argon/nitromethane samples, allowing researchers to access low-temperature states/phases of matter (without sample heating). These states cannot ordinarily be accessed during static isothermal or high-power, single-laser-pulse compression experiments. This is important, for instance, in the study of low-Z materials present at depth within gas giant planets or ice-moons. Nano-shocking with short-pulse lasers continues to be a useful technique to enhance the ultimate dynamic compression of samples—without over-shocking the sample or converting the shock energy to heat.

The concept of pre-compressing a sample within a DAC and then subjecting it to ***double pulse compression (DPC)***, or ***RPC*** was initially suggested by Kimura et al. in 2010 [22]. RPC was subsequently implemented in 2012 by Rygg et al., who subjected a variety of targets to ramped pulses with ramp rates of 5 TW/cm^2-s. This generated a more gradual compression instead of an intense shock. The result was that samples were compressed to much higher pressures (up to 900 GPa) with minimal shock heating. Rygg and associates demonstrated that Fe, Cu, Sn, Ta, Pb, Zr, C, and MgO could all be isentropically compressed in this manner [49]. RPC also makes it possible to prevent materials from melting prematurely during compression, allowing low-temperature compressed states and phases to be

investigated [49]. These important improvements of nano-shocking, DPC, and RPC can be seen in the middle of Figure 8's timeline.

Another useful experiment in this timeframe was the investigation of high-pressure phases of magnesium oxide (MgO), a common mineral in terrestrial planets, which is also thought to be present in super-Earths, much more massive than Earth (>1 M_e). Coppari et al. observed an important solid–solid phase transition between the B1-phase (rocksalt crystal structure) and the B2-phase (caesium chloride structure) of MgO, at 400–600 GPa and observed that the B2 phase was stable up to 900 GPa for the first time [30]. Laser pulse compression occurred over a few nanoseconds. Pressures of 600 GPa are anticipated deep within the interior of super-earths with masses >5 M_e, so this work helped predict the internal structure/dynamics of large rocky planets with MgO outside our solar system.

Perhaps the most extreme LDC–DAC experiment to date is that of Crandall et al. in 2020, which achieved a dynamic compression of about 1 TPa and temperatures of up to 93,000 K [27]. They pre-compressed carbon dioxide samples to 1.16 GPa inside a DAC, and then shock-compressed the liquid or solid CO_2 samples to extreme conditions using the Omega Laser at 351 nm. A configuration similar to that of Figure 2A was used, only with quartz witness plates and a sapphire anvil on the back side. One objective of the experiment was to identify the transition to (and properties of) anticipated metallic phases of CO_2, which occurs at/above 100 GPa and 9000 K. During this experiment, Crandall et al. were able to extend the EOS for CO_2 into this extreme regime. All this information is valuable for better modelling of warm, dense (molecular) matter, such as is likely extant in large gas giant planets and brown dwarfs.

In 2021, the C-O-H system was studied by Kadobayashi et al. Using the LDC–DAC approach with hydrocarbon precursors, they found a new route to diamond at less extreme temperatures (13–45 GPa, 1600 K) than had previously been observed (10–150 GPa, 2000–5000 K) [198,237–240]. This work provided an important contribution because the authors observed rapid reaction rates at 1600 K (a useful synthetic route to diamond), and because it demonstrated that diamond will likely form within the mantles of icy planets (e.g., Uranus and Neptune)—and "rain" diamond within the icy planets' interiors.

Recently, Brygoo et al. explored the immiscibility of hydrogen and helium at high pressures for the first time [60]. They initially pre-compressed homogeneous H–He mixtures to about 4 GPa at 300 K, then laser shock compressed the samples using a configuration similar to Figure 2D. The H–He mixture was pressurised to approximately 93 GPa and heated to 4700 K. These conditions are similar to warm, dense matter conditions deep inside gas giants such as Jupiter (See Figure 3). They discovered that the H–He combination is immiscible over a range of pressures and temperatures (to the right of a line crossing 100 GPa and 4000 K); the implication is that gas giants are likely to have layered interiors that are driven by this H–He immiscibility.

In addition to these highlighted works, Tables 1 and 2 (below) provide a summary of the many materials/minerals that have been modified or studied using laser dynamic compression diamond anvil cell methods. Much of this prior research has been focused on the determination of EOS and phase transitions relevant to the geological and planetary sciences. Table 1 focuses on low-Z Fluids studied/modified during LDC–DAC studies which are relevant to planetary science and astrophysics, while Table 2 gives the higher-Z minerals/materials that are typically pertinent to geo-physics and advanced materials science.

5. Conclusions and Future Work

This article has assessed the rapid development of laser-induced dynamic compression in diamond anvil cell methods over the past two decades, providing a summary of the primary methods employed, underlying physics present, history of key developmental events, and tables of relevant materials processing experiments attempted to date. It is clear that LDC–DAC experiments allow researchers to access a (dynamic) pressure regime that is not otherwise accessible for study (10 GPa–900+ GPa without significant heating)—and the experiments conducted up until now have only begun to access the potential physical

states and materials that will be generated by this technique. The use of pre-compression within the DAC allows researchers to control the initial and final conditions applied to a sample, with dynamic compression, allowing the retention of metastable phases.

In the medium-term, LDC–DAC methods provide a practical means of evaluating material transformations/stability over a wide range of potential shock conditions; this has application to the development of shock-resistant materials/structures that withstand damage in extreme environments. Applications include fusion energy containment, rocket engine development, and fabrication of high-energy laser optics. A wide variety of aerospace, military, and commercial applications have been proposed [241–244].

At present, the LDC–DAC method also remains the only approach available to explore extreme environments present within moon-, dwarf-planet-, and planetary-interiors. We know very little about the internal structure and dynamics of these bodies, which depends largely on the properties/phases of the materials present at these pressures/temperatures. For example low-Z materials including water, ammonia, and methane were explored by LDC–DAC systems to determine their EOS [22]. Furthermore, many other important materials can be also characterised by this technique such as quartz, garnet, and complex mixtures of water, ethanol, and ammonia [245–247].

The door is wide open to study materials other than those explored in Tables 1 and 2. For example, ZnO, some nonlinear optical (NLO) single crystals, L-alanine doped potassium dihydrogen orthophosphate, semiconductor microsystems materials and photonic crystals (electromagnetic band gap materials)—all these materials show potential for high stability under shockwave impact in terms of physical, mechanical, and chemical properties, yet they are still unknown in how they are going to react under pre-compressed and shocking conditions [243,244,248–250]. The proof of stability under these conditions will serve the vast applications of shockwave-stable materials such as aerospace, optical modulation and data storage and micro-electromechanical systems.

The potential for the synthesis of novel metastable materials, e.g., lonsdaleite [251–253], lechatelierite quartz [254–256], and similar shocked materials [69,257–259] using the LDC–DAC technique cannot be overstated. Originally discovered in the rocks surrounding meteorite impacts, high-quality lonsdaleite has been somewhat elusive to synthesise in larger quantities. Yet, this material has been predicted to exhibit a hardness greater than diamond [260]. LDC–DAC experiments provide a controlled environment for determining optimal synthesis conditions for such materials; these conditions can then be applied to a range of processes, including those most conducive to bulk synthesis. This has the potential to open an entirely new field of materials research, especially if novel methods of processing many anvil cells in parallel can be realised— with benefit similar to combinational chemistry [261]. Much more work should be conducted in this area.

In the longer term, significant fundamental contributions may be realised through augmented LDC–DAC experimentation. For example, Kimura et al. suggest that, at pressures approaching 100 TPa, it may be possible to obtain an entirely new regime of chemistry; at such extreme pressures, compression forces exceed the strength of outer electron shells, allowing for interactions (and bonding) between adjacent atom's inner electron orbitals for the first time; this type of chemical bonding has yet to be explored experimentally [22,69]. Consider the potential for novel metastable material synthesis and/or increased understanding of geological and planetary dynamics.

In the future, it is also anticipated that the use of new techniques, e.g., the use of high-power, short-pulse lasers, will add significantly to the diversity of experimental results obtained and the types of material processing/modification that will be achieved. In order to use such ultrashort laser pulses, novel experimental methods will be needed, such as greater thinning of the diamond anvil to minimise back-rarefraction, improved impedance matching at interfaces, and beam shaping to minimise side rarefraction of the shockwave [58]. In addition, novel methods of ramped and modulated-pulse compression will likely provide greater control of the peak pressures obtained.

Author Contributions: Conceptualisation, M.E.A. and J.L.M.; methodology, M.E.A.; investigation, M.E.A.; resources, M.E.A.; data curation, M.E.A.; writing—original draft preparation, M.E.A.; proofreading—review and editing, M.E.A., W.D.M., V.T. and J.L.M.; visualisation, M.E.A.; supervision, J.L.M.; project administration, J.L.M. All authors have read and agreed to the published version of the manuscript.

Funding: Funding provided by La Trobe University Research Infrastructure Fund.

Data Availability Statement: Not applicable.

Acknowledgments: We would like to thank the La Trobe University Research Infrastructure Fund for their generous support of fundamental high-pressure research within the EϵMC^2 Labs. This work is dedicated to our parents and grandparents, who have greatly supported us in our education and research endeavours.

Conflicts of Interest: The authors declare no conflict of interest. The funders had no role in the design of the study; in the collection, analyses, or interpretation of data; in the writing of the manuscript; or in the decision to publish the results.

Appendix A

Table A1. Summary of all research papers that result from the key search words in two main scientific databases.

Keyword / Database/Date	ScienceDirect	Web of Science	Final Access Date
Diamond Anvil Cell	8432	7294	2 August 2022
Laser diamond anvil cell	1466	1369	2 August 2022
(ALL = (Laser diamond anvil cell)) NOT ALL = (synchrotron)	1291	783	2 August 2022
Diamond anvil cell AND "Laser heated"	703	766	2 August 2022
(ALL = (Laser diamond anvil cell AND (React * OR chemical reaction OR synthe *)))	430	407	2 August 2022
(ALL = (Laser diamond anvil cell AND (shock * OR shockwave * OR pressure wave OR dynamic compression)))	66	157	2 August 2022
(ALL = (Laser diamond anvil cell AND (spectroscop *)) NOT ALL = (X-ray))	163	150	2 August 2022

* In addition to the listed keywords, authors and research groups were also searched forward and backward from each of the 27 works. Additionally, some alternative keywords were searched.

References

1. Bassett, W.A. The birth and development of laser heating in diamond anvil cells. *Rev. Sci. Instrum.* **2001**, *72*, 1270–1272. [CrossRef]
2. Bridgman, P.W. Polymorphism, Principally of the Elements, up to 50,000 kg/cm^2. *Phys. Rev.* **1935**, *48*, 893–906. [CrossRef]
3. Hemley, R.J.; Percy, W. Bridgman's second century. *High Pressure Res.* **2010**, *30*, 581–619. [CrossRef]
4. Sahu, P.C.; Chandra Shekar, N.V. High pressure research on materials. *Resonance* **2007**, *12*, 49–64. [CrossRef]
5. Ren, D.; Li, H. A Review of High-Temperature and High-Pressure Experimental Apparatus Capable of Generating Differential Stress. *Front. Earth Sci.* **2022**, *10*, 852403. [CrossRef]
6. Bassett, W.A. Diamond anvil cell, 50th birthday. *High Pressure Res.* **2009**, *29*, 163–186. [CrossRef]
7. Alabdulkarim, M.E.; Maxwell, W.D.; Thapliyal, V.; Maxwell, J.L. A Comprehensive Review of High-Pressure Laser-Induced Materials Processing, Part I: Laser-Heated Diamond Anvil Cells. *J. Manuf. Mater. Process.* **2022**, *6*, 111. [CrossRef]
8. Saxena, S.K.; Dubrovinsky, L.S.; Häggkvist, P.; Cerenius, Y.; Shen, G.; Mao, H.K. Synchrotron X-Ray Study of Iron at High Pressure and Temperature. *Science* **1995**, *269*, 1703–1704. [CrossRef]
9. Andrault, D.; Fiquet, G. Synchrotron radiation and laser heating in a diamond anvil cell. *Rev. Sci. Instrum.* **2001**, *72*, 1283–1288. [CrossRef]
10. Hemley, R.J.; Mao, H.-K.; Struzhkin, V.V. Synchrotron radiation and high pressure: New light on materials under extreme conditions. *J. Synchrotron Radiat.* **2005**, *12*, 135–154. [CrossRef]
11. Kavner, A.; Panero, W.R. Temperature gradients and evaluation of thermoelastic properties in the synchrotron-based laser-heated diamond cell. *Phys. Earth Planet. Inter.* **2004**, *143–144*, 527–539. [CrossRef]
12. Duffy, T.S. Synchrotron facilities and the study of the Earth's deep interior. *Rep. Prog. Phys.* **2005**, *68*, 1811–1859. [CrossRef]
13. Boehler, R.; Musshoff, H.G.; Ditz, R.; Aquilanti, G.; Trapananti, A. Portable laser-heating stand for synchrotron applications. *Rev. Sci. Instrum.* **2009**, *80*, 045103. [CrossRef]

14. Piermarini, G.J. High pressure X-ray crystallography with the diamond cell at NIST/NBS. *J. Res. Nat. Inst. Stand. Technol.* **2001**, *106*, 889. [CrossRef]
15. Zimmerman, A.M. High-Pressure Studies in Cell Biology. In *International Review of Cytology*; Bourne, G.H., Danielli, J.F., Jeon, K.W., Eds.; Academic Press: Cambridge, MA, USA, 1971; Volume 30, pp. 1–47.
16. O'Bannon, E.F.; Jenei, Z.; Cynn, H.; Lipp, M.J.; Jeffries, J.R. Contributed Review: Culet diameter and the achievable pressure of a diamond anvil cell: Implications for the upper pressure limit of a diamond anvil cell. *Rev. Sci. Instrum.* **2018**, *89*, 111501. [CrossRef]
17. Zhao, D.; Wang, M.; Xiao, G.; Zou, B. Thinking about the Development of High-Pressure Experimental Chemistry. *J. Phys. Chem. Lett.* **2020**, *11*, 7297–7306. [CrossRef]
18. Akimoto, S.-i. High-Pressure Research in Geophysics: Past, Present and Future. In *High-Pressure Research in Mineral Physics: A Volume in Honor of Syun-iti Akimoto*; Terra Scientific Publishing Company: Tokyo, Japan, 1987; pp. 1–13.
19. Falk, K. Experimental methods for warm dense matter research. *High Power Laser Sci. Eng.* **2018**, *6*, e59. [CrossRef]
20. Duffy, T.S.; Smith, R.F. Ultra-High Pressure Dynamic Compression of Geological Materials. *Front. Earth Sci.* **2019**, *7*, 23. [CrossRef]
21. Loubeyre, P.; Celliers, P.M.; Hicks, D.G.; Henry, E.; Dewaele, A.; Pasley, J.; Eggert, J.; Koenig, M.; Occelli, F.; Lee, K.M.; et al. Coupling static and dynamic compressions: First measurements in dense hydrogen. *High Pressure Res.* **2004**, *24*, 25–31. [CrossRef]
22. Kimura, T.; Ozaki, N.; Okuchi, T.; Terai, T.; Sano, T.; Shimizu, K.; Sano, T.; Koenig, M.; Hirose, A.; Kakeshita, T.; et al. Significant static pressure increase in a precompression cell target for laser-driven advanced dynamic compression experiments. *Phys. Plasma* **2010**, *17*, 054502. [CrossRef]
23. Dubrovinskaia, N.; Dubrovinsky, L.; Solopova Natalia, A.; Abakumov, A.; Turner, S.; Hanfland, M.; Bykova, E.; Bykov, M.; Prescher, C.; Prakapenka Vitali, B.; et al. Terapascal static pressure generation with ultrahigh yield strength nanodiamond. *Sci. Adv.* **2016**, *2*, e1600341. [CrossRef] [PubMed]
24. Armstrong, M.R.; Crowhurst, J.C.; Bastea, S.; Zaug, J.M. Ultrafast observation of shocked states in a precompressed material. *J. Appl. Phys.* **2010**, *108*, 023511. [CrossRef]
25. Moon, S.J.; Cauble, R.; Collins, G.W.; Celliers, P.M.; Hicks, D.; Da Silva, L.B.; Mackinon, A.; Wallace, R.; Hammel, B.; Hsing, W.; et al. *Experimental Design for Laser Produced Shocks in Diamond Anvil Cells*; US Department of Energy (US): Atlanta, GA, USA, 2001. Available online: https://www.osti.gov/biblio/15002090 (accessed on 9 October 2022).
26. Lee, K.K.M.; Benedetti, L.R.; Jeanloz, R.; Celliers, P.M.; Eggert, J.H.; Hicks, D.G.; Moon, S.J.; Mackinnon, A.; Da Silva, L.B.; Bradley, D.K.; et al. Laser-driven shock experiments on precompressed water: Implications for "icy" giant planets. *J. Chem. Phys.* **2006**, *125*, 014701. [CrossRef] [PubMed]
27. Crandall, L.E.; Rygg, J.R.; Spaulding, D.K.; Boehly, T.R.; Brygoo, S.; Celliers, P.M.; Eggert, J.H.; Fratanduono, D.E.; Henderson, B.J.; Huff, M.F.; et al. Equation of State of CO_2 Shock Compressed to 1 TPa. *Phys. Rev. Lett.* **2020**, *125*, 165701. [CrossRef] [PubMed]
28. Loubeyre, P.; Brygoo, S.; Eggert, J.; Celliers, P.M.; Spaulding, D.K.; Rygg, J.R.; Boehly, T.R.; Collins, G.W.; Jeanloz, R. Extended data set for the equation of state of warm dense hydrogen isotopes. *Phys. Rev. B: Condens. Matter* **2012**, *86*, 144115. [CrossRef]
29. Shu, H.; Li, J.; Tu, Y.; Ye, J.; Wang, J.; Zhang, Q.; Tian, H.; Jia, G.; He, Z.; Zhang, F.; et al. Measurement of the sound velocity of shock compressed water. *Sci. Rep.* **2021**, *11*, 6116. [CrossRef]
30. Coppari, F.; Smith, R.F.; Eggert, J.H.; Wang, J.; Rygg, J.R.; Lazicki, A.; Hawreliak, J.A.; Collins, G.W.; Duffy, T.S. Experimental evidence for a phase transition in magnesium oxide at exoplanet pressures. *Nat. Geosci.* **2013**, *6*, 926–929. [CrossRef]
31. McGonegle, D.; Heighway, P.G.; Sliwa, M.; Bolme, C.A.; Comley, A.J.; Dresselhaus-Marais, L.E.; Higginbotham, A.; Poole, A.J.; McBride, E.E.; Nagler, B.; et al. Investigating off-Hugoniot states using multi-layer ring-up targets. *Sci. Rep.* **2020**, *10*, 13172. [CrossRef]
32. Rao, U.; Chaurasia, S.; Mishra, A.K.; Pasley, J. Phase transitions in benzene under dynamic and static compression. *J. Raman Spectrosc.* **2021**, *52*, 770–781. [CrossRef]
33. Rapp, L.; Haberl, B.; Pickard, C.J.; Bradby, J.E.; Gamaly, E.G.; Williams, J.S.; Rode, A.V. Experimental evidence of new tetragonal polymorphs of silicon formed through ultrafast laser-induced confined microexplosion. *Nat. Commun.* **2015**, *6*, 7555. [CrossRef]
34. Juodkazis, S.; Kohara, S.; Ohishi, Y.; Hirao, N.; Vailionis, A.; Mizeikis, V.; Saito, A.; Rode, A. Structural changes in femtosecond laser modified regions inside fused silica. *J. Opt.* **2010**, *12*, 124007. [CrossRef]
35. Spaulding, D.K. *Laser-Driven Shock Compression Studies of Planetary Compositions*; ProQuest Dissertations Publishing: Ann Arbor, MI, USA, 2010.
36. Lazicki, A.; McGonegle, D.; Rygg, J.R.; Braun, D.G.; Swift, D.C.; Gorman, M.G.; Smith, R.F.; Heighway, P.G.; Higginbotham, A.; Suggit, M.J.; et al. Metastability of diamond ramp-compressed to 2 terapascals. *Nature* **2021**, *589*, 532–535. [CrossRef]
37. Smith, R.F.; Eggert, J.H.; Jeanloz, R.; Duffy, T.S.; Braun, D.G.; Patterson, J.R.; Rudd, R.E.; Biener, J.; Lazicki, A.E.; Hamza, A.V.; et al. Ramp compression of diamond to five terapascals. *Nature* **2014**, *511*, 330–333. [CrossRef]
38. Kim, D.; Smith, R.F.; Ocampo, I.K.; Coppari, F.; Marshall, M.C.; Ginnane, M.K.; Wicks, J.K.; Tracy, S.J.; Millot, M.; Lazicki, A.; et al. Structure and density of silicon carbide to 1.5 TPa and implications for extrasolar planets. *Nat. Commun.* **2022**, *13*, 2260. [CrossRef]
39. Bachmann, B.; Kritcher, A.L.; Benedetti, L.R.; Falcone, R.W.; Glenn, S.; Hawreliak, J.; Izumi, N.; Kraus, D.; Landen, O.L.; Le Pape, S.; et al. Using penumbral imaging to measure micrometer size plasma hot spots in Gbar equation of state experiments on the National Ignition Facility. *Rev. Sci. Instrum.* **2014**, *85*, 11D614. [CrossRef]

40. Kritcher, A.L.; Döppner, T.; Swift, D.; Hawreliak, J.; Collins, G.; Nilsen, J.; Bachmann, B.; Dewald, E.; Strozzi, D.; Felker, S.; et al. Probing matter at Gbar pressures at the NIF. *High Energy Density Phys.* **2014**, *10*, 27–34. [CrossRef]
41. Sistrunk, E.; Alessi, D.; Bayramian, A.J.; Chesnut, K.D.; Erlandson, A.C.; Galvin, T.C.; Gibson, D.; Nguyen, H.T.; Reagan, B.A.; Schaffers, K.I.; et al. Laser Technology Development for High Peak Power Lasers Achieving Kilowatt Average Power and Beyond. *Proc. SPIE* **2019**, *11034*, 1103407. [CrossRef]
42. Crawford, D.; Thiagarajan, P.; Goings, J.; Caliva, B.; Smith, S.; Walker, R. Advancements of ultra-high peak power laser diode arrays. *Proc. SPIE* **2018**, *10514*, 105140H. [CrossRef]
43. Xia, J.; Dong, X.; Yuan, H. Generation of High Peak Power Pulses With Controllable Repetition Rate in Doubly Q-Switched Laser With AOM/$SnSe_2$. *Front. Phys.* **2022**, *10*, 213. [CrossRef]
44. Chvykov, V. *New Generation of Ultra-High Peak and Average Power Laser Systems*; IntechOpen: London, UK, 2018.
45. Brasch, J.W.; Melveger, A.J.; Lippincott, E.R. Laser excited Raman spectra of samples under very high pressures. *Chem. Phys. Lett.* **1968**, *2*, 99–100. [CrossRef]
46. Crandall, L.E.; Rygg, J.R.; Spaulding, D.K.; Huff, M.F.; Marshall, M.C.; Polsin, D.N.; Jeanloz, R.; Boehly, T.R.; Zaghoo, M.; Henderson, B.J.; et al. Equation-of-state, sound speed, and reshock of shock-compressed fluid carbon dioxide. *Phys. Plasma* **2021**, *28*, 022708. [CrossRef]
47. Eggert, J.; Brygoo, S.; Loubeyre, P.; McWilliams, R.S.; Celliers, P.M.; Hicks, D.G.; Boehly, T.R.; Jeanloz, R.; Collins, G.W. Hugoniot Data for Helium in the Ionization Regime. *Phys. Rev. Lett.* **2008**, *100*, 124503. [CrossRef]
48. Boehly, T.R.; Hicks, D.G.; Celliers, P.M.; Collins, T.J.B.; Earley, R.; Eggert, J.H.; Jacobs-Perkins, D.; Moon, S.J.; Vianello, E.; Meyerhofer, D.D.; et al. Properties of fluid deuterium under double-shock compression to several Mbar. *Phys. Plasma* **2004**, *11*, L49–L52. [CrossRef]
49. Rygg, J.R.; Eggert, J.H.; Lazicki, A.E.; Coppari, F.; Hawreliak, J.A.; Hicks, D.G.; Smith, R.F.; Sorce, C.M.; Uphaus, T.M.; Yaakobi, B.; et al. Powder diffraction from solids in the terapascal regime. *Rev. Sci. Instrum.* **2012**, *83*, 113904. [CrossRef] [PubMed]
50. Lee, K.K.M.; Benedetti, L.R.; Mackinnon, A.; Hicks, D.; Moon, S.J.; Loubeyre, P.; Occelli, F.; Dewaele, A.; Collins, G.W.; Jeanloz, R. Taking Thin Diamonds to Their Limit: Coupling Static-Compression and Laser-Shock Techniques to Generate Dense Water. *AIP Conf. Proc.* **2002**, *620*, 1363–1366. [CrossRef]
51. Henry, E.; Brygoo, S.; Loubeyre, P.; Koenig, M.; Benuzzi-Mounaix, A.; Ravasio, A.; Vinci, T. Laser-driven shocks in precompressed water samples. *J. Phys. IV France* **2006**, *133*, 1093–1095. [CrossRef]
52. Eggert, J.H.; Celliers, P.M.; Hicks, D.G.; Rygg, J.R.; Collins, G.W.; Brygoo, S.; Loubeyre, P.; McWilliams, R.S.; Spaulding, D.; Jeanloz, R.; et al. Shock Experiments on Pre-Compressed Fluid Helium. *AIP Conf. Proc.* **2009**, *1161*, 26–31. [CrossRef]
53. LLNL; Bastea; Zaug, J. Shocking Results from Diamond Anvil Cell Experiments. Available online: https://www.llnl.gov/news/shocking-results-diamond-anvil-cell-experiments (accessed on 1 November 2022).
54. Benuzzi-Mounaix, A.; Koenig, M.; Huser, G.; Faral, B.; Grandjouan, N.; Batani, D.; Henry, E.; Tomasini, M.; Hall, T.A.; Guyot, F. Generation of a double shock driven by laser. *Phys. Rev. E Stat. Nonlin. Soft Matter Phys.* **2004**, *70*, 045401. [CrossRef]
55. Guarguaglini, M.; Hernandez, J.A.; Benuzzi-Mounaix, A.; Bolis, R.; Brambrink, E.; Vinci, T.; Ravasio, A. Characterizing equation of state and optical properties of dynamically pre-compressed materials. *Phys. Plasma* **2019**, *26*, 042704. [CrossRef]
56. Sollier, A.; Auroux, E.; Vauthier, J.S.; Boustie, M.; He, H.; de Rességuier, T.; Berterretche, P.; Desbiens, N.; Bourasseau, E.; Maillet, J.B. A New Experimental Design for Laser-Driven Shocks On Precompressed And Preheated Water Samples. *AIP Conf. Proc.* **2007**, *955*, 1192–1195. [CrossRef]
57. Jeanloz, R.; Celliers, P.M.; Collins, G.W.; Eggert, J.H.; Lee, K.K.M.; McWilliams, R.S.; Brygoo, S.; Loubeyre, P. Achieving high-density states through shock-wave loading of precompressed samples. *Proc. Natl. Acad. Sci. USA* **2007**, *104*, 9172–9177. [CrossRef]
58. Nissim, N.; Eliezer, S.; Werdiger, M.; Perelmutter, L. Approaching the "cold curve" in laser-driven shock wave experiment of a matter precompressed by a partially perforated diamond anvil. *Laser Part. Beams* **2013**, *31*, 73–79. [CrossRef]
59. Brygoo, S.; Millot, M.; Loubeyre, P.; Lazicki, A.E.; Hamel, S.; Qi, T.; Celliers, P.M.; Coppari, F.; Eggert, J.H.; Fratanduono, D.E.; et al. Analysis of laser shock experiments on precompressed samples using a quartz reference and application to warm dense hydrogen and helium. *J. Appl. Phys.* **2015**, *118*, 195901. [CrossRef]
60. Brygoo, S.; Loubeyre, P.; Millot, M.; Rygg, J.R.; Celliers, P.M.; Eggert, J.H.; Jeanloz, R.; Collins, G.W. Evidence of hydrogen–helium immiscibility at Jupiter-interior conditions. *Nature* **2021**, *593*, 517–521. [CrossRef]
61. Kimura, T. Application of Laser Technology for Static and Dynamic Compression Experiments. *Rev. High Press. Sci. Technol.* **2018**, *28*, 131–138. [CrossRef]
62. Neff, S.; Martinez, D.; Plechaty, C.; Stein, S.; Presura, R. Developing flyer plate impact experiments for shockwave interaction studies. In Proceedings of the 2010 Abstracts IEEE International Conference on Plasma Science, IEEE, Norfolk, VA, USA, 20–24 June 2010. [CrossRef]
63. Neff, S.; Presura, R. Simulation of shock waves in flyer plate impact experiments. *Laser Part. Beams* **2010**, *28*, 539–545. [CrossRef]
64. Schram, D.C.; Mazouffre, S.; Engeln, R.; van de Sanden, M.C.M. The Physics of Plasma Expansion. In *Atomic and Molecular Beams: The State of the Art 2000*; Campargue, R., Ed.; Springer: Berlin/Heidelberg, Germany, 2001; pp. 209–235.
65. Eliezer, S. *The Interaction of High-Power Lasers with Plasmas*; Institute of Physics Publishing: Bristol, UK, 2002.
66. Itoh, S. CHAPTER 3.2—Shock Waves in Liquids. In *Handbook of Shock Waves*; Ben-Dor, G., Igra, O., Elperin, T.O.V., Eds.; Academic Press: Burlington, NJ, USA, 2001; pp. 263–314.

67. Sakakura, M.; Terazima, M.; Shimotsuma, Y.; Miura, K.; Hirao, K. Observation of pressure wave generated by focusing a femtosecond laser pulse inside a glass. *Opt. Express* **2007**, *15*, 5674–5686. [CrossRef]
68. Henderson, L.R.F. CHAPTER 2—General Laws for Propagation of Shock Waves Through Matter. In *Handbook of Shock Waves*; Ben-Dor, G., Igra, O., Elperin, T.O.V., Eds.; Academic Press: Burlington, NJ, USA, 2001; pp. 143–183.
69. Hamilton, B.W.; Sakano, M.N.; Li, C.; Strachan, A. Chemistry Under Shock Conditions. *Annu. Rev. Mater. Res.* **2021**, *51*, 101–130. [CrossRef]
70. Williams, Q.; Knittle, E.; Jeanloz, R. The high-pressure melting curve of iron: A technical discussion. *J. Geophys. Res. Solid Earth* **1991**, *96*, 2171–2184. [CrossRef]
71. Woollam, J.A.; Chu, C.W. *High-Pressure and Low-Temperature Physics*; Springer: New York, NY, USA, 2012.
72. French, M.; Becker, A.; Lorenzen, W.; Nettelmann, N.; Bethkenhagen, M.; Wicht, J.; Redmer, R. Ab Initio Simulations for Material Properties Along the Jupiter Adiabat. *Astrophys. J. Suppl. ApJS* **2012**, *202*, 5. [CrossRef]
73. Nissim, N.; Eliezer, S.; Werdiger, M. The sound velocity throughout the P-ρ phase-space with application to laser induced shock wave in matter precompressed by a diamond anvil cell. *J. Appl. Phys.* **2014**, *115*, 213503. [CrossRef]
74. Millot, M.; Hamel, S.; Rygg, J.R.; Celliers, P.M.; Collins, G.W.; Coppari, F.; Fratanduono, D.E.; Jeanloz, R.; Swift, D.C.; Eggert, J.H. Experimental evidence for superionic water ice using shock compression. *Nature Physics* **2018**, *14*, 297–302. [CrossRef]
75. Yoo, C.-S.; Wei, H.; Dias, R.; Shen, G.; Smith, J.; Chen, J.-Y.; Evans, W. Time-Resolved Synchrotron X-ray Diffraction on Pulse Laser Heated Iron in Diamond Anvil Cell. *J. Phys. Conf. Ser.* **2012**, *377*, 012108. [CrossRef]
76. Dewaele, A.; Mezouar, M.; Guignot, N.; Loubeyre, P. High melting points of tantalum in a laser-heated diamond anvil cell. *Phys. Rev. Lett.* **2010**, *104*, 255701. [CrossRef]
77. Andrault, D.; Fiquet, G.; Kunz, M.; Visocekas, F.; Häusermann, D. The Orthorhombic Structure of Iron: An in Situ Study at High-Temperature and High-Pressure. *Science* **1997**, *278*, 831–834. [CrossRef]
78. Armstrong, L.S.; Walter, M.J. Tetragonal almandine pyrope phase (TAPP): Retrograde Mg-perovskite from subducted oceanic crust? *Eur. J. Mineral.* **2012**, *24*, 587–597. [CrossRef]
79. Armstrong, L.S.; Walter, M.J.; Tuff, J.R.; Lord, O.T.; Lennie, A.R.; Kleppe, A.K.; Clark, S.M. Perovskite Phase Relations in the System CaO–MgO–TiO_2–SiO_2 and Implications for Deep Mantle Lithologies. *J. Petrol.* **2012**, *53*, 611–635. [CrossRef]
80. Benedetti, L.R.; Loubeyre, P. Temperature gradients, wavelength-dependent emissivity, and accuracy of high and very-high temperatures measured in the laser-heated diamond cell. *High Pressure Res.* **2004**, *24*, 423–445. [CrossRef]
81. Boehler, R. Melting of the FeFeO and the FeFeS systems at high pressure: Constraints on core temperatures. *Earth Planet. Sci. Lett.* **1992**, *111*, 217–227. [CrossRef]
82. Boehler, R. Temperatures in the Earth's core from melting-point measurements of iron at high static pressures. *Nature* **1993**, *363*, 534–536. [CrossRef]
83. Boehler, R.; Ross, M.; Boercker, D.B. High-pressure melting curves of alkali halides. *Phys. Rev. B Condens. Matter* **1996**, *53*, 556–563. [CrossRef]
84. Boehler, R.; Chopelas, A. A new approach to laser heating in high pressure mineral physics. *Geophys. Res. Lett.* **1991**, *18*, 1147–1150. [CrossRef]
85. Boehler, R.; Ross, M.; Boercker, D.B. Melting of LiF and NaCl to 1 Mbar: Systematics of Ionic Solids at Extreme Conditions. *Phys. Rev. Lett.* **1997**, *78*, 4589–4592. [CrossRef]
86. Bolfan-Casanova, N.; Andrault, D.; Amiguet, E.; Guignot, N. Equation of state and post-stishovite transformation of Al-bearing silica up to 100GPa and 3000K. *Phys. Earth Planet. Inter.* **2009**, *174*, 70–77. [CrossRef]
87. Meade, C.; Mao, H.K.; Hu, J. High-Temperature Phase Transition and Dissociation of (Mg, Fe)SiO_3 Perovskite at Lower Mantle Pressures. *Science* **1995**, *268*, 1743–1745. [CrossRef]
88. Dewaele, A.; Mezouar, M.; Guignot, N.; Loubeyre, P. Melting of lead under high pressure studied using second-scale time-resolved x-ray diffraction. *Phys. Rev. B Condens. Matter* **2007**, *76*, 144106. [CrossRef]
89. Dewaele, A.; Belonoshko, A.B.; Garbarino, G.; Occelli, F.; Bouvier, P.; Hanfland, M.; Mezouar, M. High-pressure—High-temperature equation of state of KCl and KBr. *Phys. Rev. B Condens. Matter* **2012**, *85*, 214105. [CrossRef]
90. Dobson, D.P.; Hunt, S.A.; Ahmed, J.; Lord, O.T.; Wann, E.T.H.; Santangeli, J.; Wood, I.G.; Vočadlo, L.; Walker, A.M.; Thomson, A.R.; et al. The phase diagram of NiSi under the conditions of small planetary interiors. *Phys. Earth Planet. Inter.* **2016**, *261*, 196–206. [CrossRef]
91. Dubrovinsky, L.S.; Saxena, S.K.; Lazor, P.; Ahuja, R.; Eriksson, O.; Wills, J.M.; Johansson, B. Experimental and theoretical identification of a new high-pressure phase of silica. *Nature* **1997**, *388*, 362–365. [CrossRef]
92. Errandonea, D.; Schwager, B.; Ditz, R.; Gessmann, C.; Boehler, R.; Ross, M. Systematics of transition-metal melting. *Phys. Rev. B Condens. Matter* **2001**, *63*, 132104. [CrossRef]
93. Errandonea, D.; Somayazulu, M.; Häusermann, D.; Mao, H.K. Melting of tantalum at high pressure determined by angle dispersive x-ray diffraction in a double-sided laser-heated diamond-anvil cell. *J. Phys. Condens. Matter* **2003**, *15*, 7635–7649. [CrossRef]
94. Errandonea, D.; Boehler, R.; Japel, S.; Mezouar, M.; Benedetti, L.R. Structural transformation of compressed solid Ar: An x-ray diffraction study to 114 GPa. *Phys. Rev. B Condens. Matter* **2006**, *73*, 092106. [CrossRef]

95. Errandonea, D.; MacLeod, S.G.; Burakovsky, L.; Santamaria-Perez, D.; Proctor, J.E.; Cynn, H.; Mezouar, M. Melting curve and phase diagram of vanadium under high-pressure and high-temperature conditions. *Phys. Rev. B Condens. Matter* **2019**, *100*, 094111. [CrossRef]
96. Fedotenko, T.; Dubrovinsky, L.; Aprilis, G.; Koemets, E.; Snigirev, A.; Snigireva, I.; Barannikov, A.; Ershov, P.; Cova, F.; Hanfland, M.; et al. Laser heating setup for diamond anvil cells for in situ synchrotron and in house high and ultra-high pressure studies. *Rev. Sci. Instrum.* **2019**, *90*, 104501–104511. [CrossRef]
97. Fiquet, G.; Andrault, D. Powder X-ray diffraction under extreme conditions of pressure and temperature. *J. Synchrotron Radiat.* **1999**, *6*, 81–86. [CrossRef]
98. Fiquet, G.; Andrault, D.; Itié, J.P.; Gillet, P.; Richet, P. X-ray diffraction of periclase in a laser-heated diamond-anvil cell. *Phys. Earth Planet. Inter.* **1996**, *95*, 1–17. [CrossRef]
99. Fiquet, G.; Dewaele, A.; Andrault, D.; Kunz, M.; Le Bihan, T. Thermoelastic properties and crystal structure of $MgSiO_3$ perovskite at lower mantle pressure and temperature conditions. *Geophys. Res. Lett.* **2000**, *27*, 21–24. [CrossRef]
100. Friedrich, A.; Morgenroth, W.; Bayarjargal, L.; Juarez-Arellano, E.A.; Winkler, B.; Konôpková, Z. In situ study of the high pressure high-temperature stability field of TaN and of the compressibilities of ϑ-TaN and TaON. *High Pressure Res.* **2013**, *33*, 633–641. [CrossRef]
101. Golberg, D.; Bando, Y.; Eremets, M.; Takemura, K.; Kurashima, K.; Yusa, H. Nanotubes in boron nitride laser heated at high pressure. *Appl. Phys. Lett.* **1996**, *69*, 2045–2047. [CrossRef]
102. Heinz, D.L.; Sweeney, J.S.; Miller, P. A laser heating system that stabilizes and controls the temperature: Diamond anvil cell applications. *Rev. Sci. Instrum.* **1991**, *62*, 1568–1575. [CrossRef]
103. Hrubiak, R.; Meng, Y.; Shen, G. Microstructures define melting of molybdenum at high pressures. *Nat. Commun.* **2017**, *8*, 14562. [CrossRef]
104. Huang, X.; Li, F.; Zhou, Q.; Meng, Y.; Litasov, K.D.; Wang, X.; Liu, B.; Cui, T. Thermal equation of state of Molybdenum determined from in situ synchrotron X-ray diffraction with laser-heated diamond anvil cells. *Sci. Rep.* **2016**, *6*, 19923. [CrossRef]
105. Japel, S.; Schwager, B.; Boehler, R.; Ross, M. Melting of copper and nickel at high pressure: The role of d electrons. *Phys. Rev. Lett.* **2005**, *95*, 167801. [CrossRef]
106. Kavner, A.; Duffy, T.S. Pressure–volume–temperature paths in the laser-heated diamond anvil cell. *J. Appl. Phys.* **2001**, *89*, 1907–1914. [CrossRef]
107. Kesson, S.E.; Fitz Gerald, J.D. Partitioning of MgO, FeO, NiO, MnO and Cr_2O_3 between magnesian silicate perovskite and magnesiowüstite: Implications for the origin of inclusions in diamond and the composition of the lower mantle. *Earth Planet. Sci. Lett.* **1992**, *111*, 229–240. [CrossRef]
108. Kesson, S.E.; Fitz Gerald, J.D.; Shelley, J.M.G. Mineral chemistry and density of subducted basaltic crust at lower-mantle pressures. *Nature* **1994**, *372*, 767–769. [CrossRef]
109. Kiefer, B.; Duffy, T.S. Finite element simulations of the laser-heated diamond-anvil cell. *J. Appl. Phys.* **2005**, *97*, 114902. [CrossRef]
110. Kim, Y.-H.; Ming, L.C.; Manghnani, M.H. High-pressure phase transformations in a natural crystalline diopside and a synthetic $CaMgSi_2O_6$ glass. *Phys. Earth Planet. Inter.* **1994**, *83*, 67–79. [CrossRef]
111. Kimura, T.; Kuwayama, Y.; Yagi, T. Melting temperatures of H_2O up to 72 GPa measured in a diamond anvil cell using CO_2 laser heating technique. *J. Chem. Phys.* **2014**, *140*, 074501. [CrossRef]
112. Young-Ho, K.O.; Kyoung Hun, O.H.; Kwang Joo, K.I.M. Installation and Operation of a Double-Sided Laser Heating System for the Synthesis of Novel Materials Under Extreme Conditions. *New Phys. Sae Mulli NPSM* **2019**, *69*, 1107–1114. [CrossRef]
113. Knittle, E.; Jeanloz, R. Synthesis and Equation of State of (Mg,Fe) SiO_3 Perovskite to Over 100 Gigapascals. *Science* **1987**, *235*, 668–670. [CrossRef]
114. Kumar, N.R.; Shekar, N.V.; Sekar, M.; Subramanian, N.; Mohan, P.C.; Srinivasan, M.P.; Parameswaran, P.; Sahu, P.C. Diamond and diamond-like carbon in laser heated diamond anvil cell at 16.5 GPa and above 2000 K from pyrolitic graphite. *Indian J. Pure Appl. Phys.* **2008**, *46*, 783–787.
115. Kupenko, I.; Strohm, C.; McCammon, C.; Cerantola, V.; Glazyrin, K.; Petitgirard, S.; Vasiukov, D.; Aprilis, G.; Chumakov, A.I.; Rüffer, R.; et al. Time differentiated nuclear resonance spectroscopy coupled with pulsed laser heating in diamond anvil cells. *Rev. Sci. Instrum.* **2015**, *86*, 114501. [CrossRef] [PubMed]
116. Lavina, B.; Dera, P.; Kim, E.; Meng, Y.; Downs Robert, T.; Weck Philippe, F.; Sutton Stephen, R.; Zhao, Y. Discovery of the recoverable high-pressure iron oxide Fe_4O_5. *Proc. Natl. Acad. Sci. USA* **2011**, *108*, 17281–17285. [CrossRef] [PubMed]
117. Lazicki, A.; Dewaele, A.; Loubeyre, P.; Mezouar, M. High-pressure—Temperature phase diagram and the equation of state of beryllium. *Phys. Rev. B Condens. Matter* **2012**, *86*, 174118. [CrossRef]
118. Lin, J.-F.; Santoro, M.; Struzhkin, V.V.; Mao, H.-k.; Hemley, R.J. In situ high pressure-temperature Raman spectroscopy technique with laser-heated diamond anvil cells. *Rev. Sci. Instrum.* **2004**, *75*, 3302–3306. [CrossRef]
119. Lin, J.-F.; Sturhahn, W.; Zhao, J.; Shen, G.; Mao, H.-k.; Hemley, R.J. Absolute temperature measurement in a laser-heated diamond anvil cell. *Geophys. Res. Lett.* **2004**, *31*, L14611. [CrossRef]
120. Lin, Y.; Hu, Q.; Zhu, L.; Meng, Y. Structure and Stability of Iron Fluoride at High Pressure–Temperature and Implication for a New Reservoir of Fluorine in the Deep Earth. *Minerals* **2020**, *10*, 783. [CrossRef]
121. Liu, L.-G. A new high-pressure phase of spinel. *Earth Planet. Sci. Lett.* **1978**, *41*, 398–404. [CrossRef]
122. Liu, L.-g. High pressure $NaAlSiO_4$: The first silicate calcium ferrite isotype. *Geophys. Res. Lett.* **1977**, *4*, 183–186. [CrossRef]

123. Liu, J.; Wang, C.; Lv, C.; Su, X.; Liu, Y.; Tang, R.; Chen, J.; Hu, Q.; Mao, H.-K.; Mao, W.L. Evidence for oxygenation of Fe-Mg oxides at mid-mantle conditions and the rise of deep oxygen. *Natl. Sci. Rev.* **2020**, *8*, 1–6. [CrossRef] [PubMed]
124. Lord, O.T.; Wann, E.T.H.; Hunt, S.A.; Walker, A.M.; Santangeli, J.; Walter, M.J.; Dobson, D.P.; Wood, I.G.; Vočadlo, L.; Morard, G.; et al. The NiSi melting curve to 70GPa. *Phys. Earth Planet. Inter.* **2014**, *233*, 13–23. [CrossRef]
125. Lord, O.T.; Wood, I.G.; Dobson, D.P.; Vočadlo, L.; Wang, W.; Thomson, A.R.; Wann, E.T.H.; Morard, G.; Mezouar, M.; Walter, M.J. The melting curve of Ni to 1 Mbar. *Earth Planet. Sci. Lett.* **2014**, *408*, 226–236. [CrossRef]
126. Meng, Y.; Shen, G.; Mao, H.K. Double-sided laser heating system at HPCAT for in situ x-ray diffraction at high pressures and high temperatures. *J. Phys. Condens. Matter* **2006**, *18*, S1097–S1103. [CrossRef]
127. Ming, L.c.; Bassett, W.A. Laser heating in the diamond anvil press up to 2000°C sustained and 3000°C pulsed at pressures up to 260 kilobars. *Rev. Sci. Instrum.* **1974**, *45*, 1115–1118. [CrossRef]
128. Miyagi, L.; Kanitpanyacharoen, W.; Raju, S.V.; Kaercher, P.; Knight, J.; MacDowell, A.; Wenk, H.-R.; Williams, Q.; Alarcon, E.Z. Combined resistive and laser heating technique for in situ radial X-ray diffraction in the diamond anvil cell at high pressure and temperature. *Rev. Sci. Instrum.* **2013**, *84*, 025118. [CrossRef]
129. Nabiei, F.; Badro, J.; Boukaré, C.; Hébert, C.; Cantoni, M.; Borensztajn, S.; Wehr, N.; Gillet, P. Investigating Magma Ocean Solidification on Earth Through Laser-Heated Diamond Anvil Cell Experiments. *Geophys. Res. Lett.* **2021**, *48*, e2021GL092446. [CrossRef]
130. Ohfuji, H.; Irifune, T.; Okada, T.; Yagi, T.; Sumiya, H. Laser heating in nano-polycrystalline diamond anvil cell. *J. Phys. Conf. Ser.* **2010**, *215*, 5. [CrossRef]
131. Ohtaka, O.; Andrault, D.; Bouvier, P.; Schultz, E.; Mezouar, M. Phase relations and equation of state of ZrO_2 to 100 GPa. *J. Appl. Crystallogr.* **2005**, *38*, 727–733. [CrossRef]
132. Panero, W.R.; Jeanloz, R. Temperature gradients in the laser-heated diamond anvil cell. *J. Geophys. Res. Solid Earth* **2001**, *106*, 6493–6498. [CrossRef]
133. Santamaría-Pérez, D.; Boehler, R. FeSi melting curve up to 70 GPa. *Earth Planet. Sci. Lett.* **2008**, *265*, 743–747. [CrossRef]
134. Pigott, J.S.; Reaman, D.M.; Panero, W.R. Microfabrication of controlled-geometry samples for the laser-heated diamond-anvil cell using focused ion beam technology. *Rev. Sci. Instrum.* **2011**, *82*, 115106. [CrossRef] [PubMed]
135. Pigott, J.S.; Velisavljevic, N.; Moss, E.K.; Draganic, N.; Jacobsen, M.K.; Meng, Y.; Hrubiak, R.; Sturtevant, B.T. Experimental melting curve of zirconium metal to 37 GPa. *J. Phys. Condens. Matter* **2020**, *32*, 355402. [CrossRef] [PubMed]
136. Polvani, D.A.; Meng, J.F.; Hasegawa, M.; Badding, J.V. Measurement of the thermoelectric power of very small samples at ambient and high pressures. *Rev. Sci. Instrum.* **1999**, *70*, 3586–3589. [CrossRef]
137. Prakapenka, V.B.; Kubo, A.; Kuznetsov, A.; Laskin, A.; Shkurikhin, O.; Dera, P.; Rivers, M.L.; Sutton, S.R. Advanced flat top laser heating system for high pressure research at GSECARS: Application to the melting behavior of germanium. *High Pressure Res.* **2008**, *28*, 225–235. [CrossRef]
138. Prakapenka, V.B.; Shen, G.; Dubrovinsky, L.S. Carbon transport in diamond anvil cells. *High Temp. High Press.* **2003**, *35/36*, 237–249. [CrossRef]
139. Raju, S.V.; Hrubiak, R.; Drozd, V.; Saxena, S. Laser-assisted processing of Ni-Al-Co-Ti under high pressure. *Mater. Manuf. Processes* **2017**, *32*, 1606–1611. [CrossRef]
140. Ross, M.; Boehler, R.; Söderlind, P. Xenon Melting Curve to 80 GPa and 5*p*-*d* Hybridization. *Phys. Rev. Lett.* **2005**, *95*, 257801. [CrossRef]
141. Runge, C.E.; Kubo, A.; Kiefer, B.; Meng, Y.; Prakapenka, V.B.; Shen, G.; Cava, R.J.; Duffy, T.S. Equation of state of $MgGeO_3$ perovskite to 65 GPa: Comparison with the post-perovskite phase. *Phys. Chem. Miner.* **2006**, *33*, 699–709. [CrossRef]
142. Sadovyi, B.; Wierzbowska, M.; Stelmakh, S.; Boccato, S.; Gierlotka, S.; Irifune, T.; Porowski, S.; Grzegory, I. Experimental and theoretical evidence of the temperature-induced wurtzite to rocksalt phase transition in GaN under high pressure. *Phys. Rev. B Condens. Matter* **2020**, *102*, 235109. [CrossRef]
143. Saha, P.; Mukherjee, G.D. Temperature measurement in double-sided laser-heated diamond anvil cell and reaction of carbon. *Indian J. Phys.* **2021**, *95*, 621–628. [CrossRef]
144. Saha, P.; Mazumder, A.; Mukherjee, G.D. Thermal conductivity of dense hcp iron: Direct measurements using laser heated diamond anvil cell. *Geosci. Front.* **2020**, *11*, 1755–1761. [CrossRef]
145. Salem, R.; Matityahu, S.; Melchior, A.; Nikolaevsky, M.; Noked, O.; Sterer, E. Image analysis of speckle patterns as a probe of melting transitions in laser-heated diamond anvil cell experiments. *Rev. Sci. Instrum.* **2015**, *86*, 093907. [CrossRef]
146. Santamaría-Pérez, D.; Ross, M.; Errandonea, D.; Mukherjee, G.D.; Mezouar, M.; Boehler, R. X-ray diffraction measurements of Mo melting to 119 GPa and the high pressure phase diagram. *J. Chem. Phys.* **2009**, *130*, 124509. [CrossRef]
147. Schultz, E.; Mezouar, M.; Crichton, W.; Bauchau, S.; Blattmann, G.; Andrault, D.; Fiquet, G.; Boehler, R.; Rambert, N.; Sitaud, B.; et al. Double-sided laser heating system for in situ high pressure–high temperature monochromatic x-ray diffraction at the esrf. *High Pressure Res.* **2005**, *25*, 71–83. [CrossRef]
148. Shen, G.; Mao, H.-k.; Hemley, R.J.; Duffy, T.S.; Rivers, M.L. Melting and crystal structure of iron at high pressures and temperatures. *Geophys. Res. Lett.* **1998**, *25*, 373–376. [CrossRef]
149. Shen, G.; Rivers, M.L.; Wang, Y.; Sutton, S.R. Laser heated diamond cell system at the Advanced Photon Source for in situ x-ray measurements at high pressure and temperature. *Rev. Sci. Instrum.* **2001**, *72*, 1273–1282. [CrossRef]

150. Shen, G.; Prakapenka, V.B.; Rivers, M.L.; Sutton, S.R. Structure of Liquid Iron at Pressures up to 58 GPa. *Phys. Rev. Lett.* **2004**, *92*, 185701. [CrossRef]
151. Shen, G.; Mao, H.-k.; Hemley, R. Laser-Heated Diamond Anvil Cell Technique: Double-Sided Heating with Multimode Nd:YAG Laser. In *Advanced Materials '96 New Trends in High Pressure Research*; Akaishi, M., Ed.; The Institute: Tsukuba, Japan, 1996.
152. Shieh, S.R.; Duffy, T.S.; Shen, G. X-ray diffraction study of phase stability in SiO2 at deep mantle conditions. *Earth Planet. Sci. Lett.* **2005**, *235*, 273–282. [CrossRef]
153. Shim, S.H.; Duffy, T.S.; Jeanloz, R.; Shen, G. Stability and crystal structure of $MgSiO_3$ perovskite to the core-mantle boundary. *Geophys. Res. Lett.* **2004**, *31*. [CrossRef]
154. Shukla, B.; Shekar, N.V.C.; Kumar, N.R.S.; Ravindran, T.R.; Sahoo, P.; Dhara, S.; Sahu, P.C. Twin chamber sample assembly in DAC and HPHT studies on GaN nano-particles. *J. Phys. Conf. Ser.* **2012**, *377*, 012014. [CrossRef]
155. Singh, A.K.; Andrault, D.; Bouvier, P. X-ray diffraction from stishovite under nonhydrostatic compression to 70GPa: Strength and elasticity across the tetragonal→orthorhombic transition. *Phys. Earth Planet. Inter.* **2012**, *208–209*, 1–10. [CrossRef]
156. Sinmyo, R.; Hirose, K. The Soret diffusion in laser-heated diamond-anvil cell. *Phys. Earth Planet. Inter.* **2010**, *180*, 172–178. [CrossRef]
157. Sinmyo, R.; Pesce, G.; Greenberg, E.; McCammon, C.; Dubrovinsky, L. Lower mantle electrical conductivity based on measurements of Al, Fe-bearing perovskite under lower mantle conditions. *Earth Planet. Sci. Lett.* **2014**, *393*, 165–172. [CrossRef]
158. Spiekermann, G.; Kupenko, I.; Petitgirard, S.; Harder, M.; Nyrow, A.; Weis, C.; Albers, C.; Biedermann, N.; Libon, L.; Sahle, C.J.; et al. A portable on-axis laser-heating system for near-90degrees X-ray spectroscopy: Application to ferropericlase and iron silicide. *J. Synchrotron Radiat.* **2020**, *27*, 414–424. [CrossRef] [PubMed]
159. Stutzmann, V.; Dewaele, A.; Bouchet, J.; Bottin, F.; Mezouar, M. High-pressure melting curve of titanium. *Phys. Rev. B Condens. Matter* **2015**, *92*, 224110. [CrossRef]
160. Auzende, A.-L.; Gillot, J.; Coquet, A.; Hennet, L.; Ona-Nguema, G.; Bonnin, D.; Esteve, I.; Roskosz, M.; Fiquet, G. Synthesis of amorphous MgO-rich peridotitic starting material for laser-heated diamond anvil cell experiments—Application to iron partitioning in the mantle. *High Pressure Res.* **2011**, *31*, 199–213. [CrossRef]
161. Tateno, S.; Hirose, K.; Ohishi, Y.; Tatsumi, Y. The Structure of Iron in Earth's Inner Core. *Science* **2010**, *330*, 359–361. [CrossRef]
162. Watanuki, T.; Shimomura, O.; Yagi, T.; Kondo, T.; Isshiki, M. Construction of laser-heated diamond anvil cell system for in situ x-ray diffraction study at SPring-8. *Rev. Sci. Instrum.* **2001**, *72*, 1289–1292. [CrossRef]
163. Weck, G.; Recoules, V.; Queyroux, J.-A.; Datchi, F.; Bouchet, J.; Ninet, S.; Garbarino, G.; Mezouar, M.; Loubeyre, P. Determination of the melting curve of gold up to 110 GPa. *Phys. Rev. B Condens. Matter* **2020**, *101*, 014106. [CrossRef]
164. Yagi, T.; Susaki, J.-I. A Laser Heating System for Diamond Anvil Using CO_2 Laser. In *High-Pressure Research: Application to Earth and Planetary Sciences*; Terra Scientific Publishing Company: Tokyo, Japan, 1992; pp. 51–54.
165. Yang, L.; Karandikar, A.; Boehler, R. Flash heating in the diamond cell: Melting curve of rhenium. *Rev. Sci. Instrum.* **2012**, *83*, 063905. [CrossRef] [PubMed]
166. Yoo, C.S.; Akella, J.; Moriarty, J.A. High-pressure melting temperatures of uranium: Laser-heating experiments and theoretical calculations. *Phys. Rev. B Condens. Matter* **1993**, *48*, 15529–15534. [CrossRef] [PubMed]
167. Yoo, C.S.; Akella, J.; Campbell, A.J.; Mao, H.K.; Hemley, R.J. Phase Diagram of Iron by in Situ X-ray Diffraction: Implications for Earth's Core. *Science* **1995**, *270*, 1473–1475. [CrossRef]
168. Yoo, C.S.; Söderlind, P.; Moriarty, J.A.; Cambell, A.J. dhcp as a possible new ϵ' phase of iron at high pressures and temperatures. *Phys. Lett. A* **1996**, *214*, 65–70. [CrossRef]
169. Yusa, H.; Takemura, K.; Matsui, Y.; Morishima, H.; Watanabe, K.; Yamawaki, H.; Aoki, K. Direct transformation of graphite to cubic diamond observed in a laser-heated diamond anvil cell. *Appl. Phys. Lett.* **1998**, *72*, 1843–1845. [CrossRef]
170. Zerr, A.; Boehler, R. Melting of (Mg, Fe)SiO_3-Perovskite to 625 Kilobars: Indication of a High Melting Temperature in the Lower Mantle. *Science* **1993**, *262*, 553–555. [CrossRef]
171. Zerr, A.; Miehe, G.; Serghiou, G.; Schwarz, M.; Kroke, E.; Riedel, R.; Fueß, H.; Kroll, P.; Boehler, R. Synthesis of cubic silicon nitride. *Nature* **1999**, *400*, 340–342. [CrossRef]
172. Zhang, L.; Meng, Y.; Mao, H.-k. Unit cell determination of coexisting post-perovskite and H-phase in (Mg,Fe)SiO_3 using multigrain XRD: Compositional variation across a laser heating spot at 119 GPa. *Prog. Earth Planet. Sci.* **2016**, *3*, 13. [CrossRef]
173. Zhang, D.; Jackson, J.M.; Zhao, J.; Sturhahn, W.; Alp, E.E.; Hu, M.Y.; Toellner, T.S.; Murphy, C.A.; Prakapenka, V.B. Temperature of Earth's core constrained from melting of Fe and $Fe_{0.9}Ni_{0.1}$ at high pressures. *Earth Planet. Sci. Lett.* **2016**, *447*, 72–83. [CrossRef]
174. Zinin, P.V.; Prakapenka, V.B.; Burgess, K.; Odake, S.; Chigarev, N.; Sharma, S.K. Combined laser ultrasonics, laser heating, and Raman scattering in diamond anvil cell system. *Rev. Sci. Instrum.* **2016**, *87*, 123908. [CrossRef]
175. Zou, G.; Ma, Y.; Mao, H.-k.; Hemley, R.J.; Gramsch, S.A. A diamond gasket for the laser-heated diamond anvil cell. *Rev. Sci. Instrum.* **2001**, *72*, 1298–1301. [CrossRef]
176. Weathers, M.S.; Bassett, W.A. Melting of carbon at 50 to 300 kbar. *Phys. Chem. Miner.* **1987**, *15*, 105–112. [CrossRef]
177. Huang, D.; Siebert, J.; Badro, J. High pressure partitioning behavior of Mo and W and late sulfur delivery during Earth's core formation. *Geochim. Cosmochim. Acta* **2021**, *310*, 19–31. [CrossRef]
178. Kurnosov, A.; Marquardt, H.; Dubrovinsky, L.; Potapkin, V. A waveguide-based flexible CO_2-laser heating system for diamond-anvil cell applications. *C.R. Geosci.* **2019**, *351*, 280–285. [CrossRef]

179. Chidester, B.A.; Thompson, E.C.; Fischer, R.A.; Heinz, D.L.; Prakapenka, V.B.; Meng, Y.; Campbell, A.J. Experimental thermal equation of state of *B2*− KCl. *Phys. Rev. B Condens. Matter* **2021**, *104*, 094107. [CrossRef]
180. Zhang, Y.; Tan, Y.; Geng, H.Y.; Salke, N.P.; Gao, Z.; Li, J.; Sekine, T.; Wang, Q.; Greenberg, E.; Prakapenka, V.B.; et al. Melting curve of vanadium up to 256 GPa: Consistency between experiments and theory. *Phys. Rev. B Condens. Matter* **2020**, *102*, 214104. [CrossRef]
181. Gaida, N.A.; Niwa, K.; Sasaki, T.; Hasegawa, M. Phase relations and thermoelasticity of magnesium silicide at high pressure and temperature. *J. Chem. Phys.* **2021**, *154*, 144701. [CrossRef]
182. Anzellini, S.; Burakovsky, L.; Turnbull, R.; Bandiello, E.; Errandonea, D. P–V–T Equation of State of Iridium Up to 80 GPa and 3100 K. *Crystals* **2021**, *11*, 452. [CrossRef]
183. Liu, L.-g. Silicate perovskite from phase transformations of pyrope-garnet at high pressure and temperature. *Geophys. Res. Lett.* **1974**, *1*, 277–280. [CrossRef]
184. Nishiyama, N.; Langer, J.; Sakai, T.; Kojima, Y.; Holzheid, A.; Gaida, N.A.; Kulik, E.; Hirao, N.; Kawaguchi, S.I.; Irifune, T.; et al. Phase relations in silicon and germanium nitrides up to 98 GPa and 2400°C. *J. Am. Ceram. Soc.* **2019**, *102*, 2195–2202. [CrossRef]
185. Bassett, W.A.; Li-Chung, M. Disproportionation of Fe_2SiO_4 to 2FeO + SiO_2 at pressures up to 250kbar and temperatures up to 3000 °C. *Phys. Earth Planet. Inter.* **1972**, *6*, 154–160. [CrossRef]
186. Kavner, A.; Jeanloz, R. The high-pressure melting curve of Allende meteorite. *Geophys. Res. Lett.* **1998**, *25*, 4161–4164. [CrossRef]
187. Boehler, R.; von Bargen, N.; Chopelas, A. Melting, thermal expansion, and phase transitions of iron at high pressures. *J. Geophys. Res. Solid Earth* **1990**, *95*, 21731–21736. [CrossRef]
188. Wakamatsu, T.; Ohta, K.; Yagi, T.; Hirose, K.; Ohishi, Y. Measurements of sound velocity in iron–nickel alloys by femtosecond laser pulses in a diamond anvil cell. *Phys. Chem. Miner.* **2018**, *45*, 589–595. [CrossRef]
189. Deemyad, S.; Sterer, E.; Barthel, C.; Rekhi, S.; Tempere, J.; Silvera, I.F. Pulsed laser heating and temperature determination in a diamond anvil cell. *Rev. Sci. Instrum.* **2005**, *76*, 125104. [CrossRef]
190. Deemyad, S.; Silvera, I.F. Melting Line of Hydrogen at High Pressures. *Phys. Rev. Lett.* **2008**, *100*, 155701. [CrossRef]
191. Yoo, C.S.; Akella, J.; Cynn, H.; Nicol, M. Direct elementary reactions of boron and nitrogen at high pressures and temperatures. *Phys. Rev. B Condens. Matter* **1997**, *56*, 140–146. [CrossRef]
192. Serghiou, G.; Miehe, G.; Tschauner, O.; Zerr, A.; Boehler, R. Synthesis of a cubic Ge_3N_4 phase at high pressures and temperatures. *J. Chem. Phys.* **1999**, *111*, 4659–4662. [CrossRef]
193. Sahu, P.C.; Takemura, K.; Yusa, H. Synthesis experiments on B-Sb, Ge-Sb, and Xe-Pd systems using a laser heated diamond anvil cell. *High Pressure Res.* **2001**, *21*, 41–50. [CrossRef]
194. Sorb, Y.A.; Subramanian, N.; Ravindran, T.R.; Sahu, P.C. High Pressure in situ Micro-Raman Spectroscopy of Ge-Sn System Synthesized in a Laser Heated Diamond Anvil Cell. *AIP Conf. Proc.* **2011**, *1349*, 1305–1306. [CrossRef]
195. Sanjay Kumar, N.R.; Chandra Shekar, N.V.; Chandra, S.; Basu, J.; Divakar, R.; Sahu, P.C. Synthesis of novel Ru_2C under high pressure–high temperature conditions. *J. Phys. Condens. Matter* **2012**, *24*, 362202. [CrossRef]
196. Fedotenko, T.; Dubrovinsky, L.; Khandarkhaeva, S.; Chariton, S.; Koemets, E.; Koemets, I.; Hanfland, M.; Dubrovinskaia, N. Synthesis of palladium carbides and palladium hydride in laser heated diamond anvil cells. *J. Alloys Compd.* **2020**, *844*, 156179. [CrossRef]
197. Gréaux, S.; Andrault, D.; Gautron, L.; Bolfan-Casanova, N.; Mezouar, M. Compressibility of $Ca_3Al_2Si3O_{12}$ perovskite up to 55 GPa. *Phys. Chem. Miner.* **2014**, *41*, 419–429. [CrossRef]
198. Zerr, A.; Serghiou, G.; Boehler, R.; Ross, M. Decomposition of alkanes at high pressures and temperatures. *High Pressure Res.* **2006**, *26*, 23–32. [CrossRef]
199. Vance, S.; Harnmeijer, J.; Kimura, J.; Hussmann, H.; deMartin, B.; Brown, J.M. Hydrothermal Systems in Small Ocean Planets. *Astrobiology* **2007**, *7*, 987–1005. [CrossRef]
200. Helled, R.; Anderson, J.D.; Podolak, M.; Schubert, G. Interior Models of Uranus and Neptune. *Astrophys. J.* **2010**, *726*, 15. [CrossRef]
201. Guillot, T.; Gautier, D. 10.13—Giant Planets. In *Treatise on Geophysics*; Schubert, G., Ed.; Elsevier: Amsterdam, The Netherlands, 2007; pp. 439–464.
202. Fossati, L.; Shulyak, D.; Sreejith, A.G.; Koskinen, T.; Young, M.E.; Cubillos, P.E.; Lara, L.M.; France, K.; Rengel, M.; Cauley, P.W.; et al. A data-driven approach to constraining the atmospheric temperature structure of the ultra-hot Jupiter KELT-9b. *Astron. Astrophys.* **2020**, *643*, A131. [CrossRef]
203. Banerjee, A.; Bernoulli, D.; Zhang, H.; Yuen, M.-F.; Liu, J.; Dong, J.; Ding, F.; Lu, J.; Dao, M.; Zhang, W.; et al. Ultralarge elastic deformation of nanoscale diamond. *Science* **2018**, *360*, 300–302. [CrossRef]
204. Ruoff, A.L. On the yield strength of diamond. *J. Appl. Phys.* **1979**, *50*, 3354–3356. [CrossRef]
205. Reinhart, W.D.; Chhabildas, L.C.; Vogler, T.J. Investigating phase transitions and strength in single-crystal sapphire using shock–reshock loading techniques. *Int. J. Impact Eng.* **2006**, *33*, 655–669. [CrossRef]
206. Bisschop, J.; den Brok, B.; Miletich, R. Brittle deformation of quartz in a diamond anvil cell. *J. Struct. Geol.* **2005**, *27*, 943–947. [CrossRef]
207. Borg, J.P.; Vogler, T.J. Mesoscale simulations of a dart penetrating sand. *Int. J. Impact Eng.* **2008**, *35*, 1435–1440. [CrossRef]
208. Dubrovinsky, L.; Khandarkhaeva, S.; Fedotenko, T.; Laniel, D.; Bykov, M.; Giacobbe, C.; Lawrence Bright, E.; Sedmak, P.; Chariton, S.; Prakapenka, V.; et al. Materials synthesis at terapascal static pressures. *Nature* **2022**, *605*, 274–278. [CrossRef] [PubMed]

209. Mao, H.K.; Bell, P.M.; Shaner, J.W.; Steinberg, D.J. Specific volume measurements of Cu, Mo, Pd, and Ag and calibration of the ruby R_1 fluorescence pressure gauge from 0.06 to 1 Mbar. *J. Appl. Phys.* **1978**, *49*, 3276–3283. [CrossRef]
210. Mostovych, A.N.; Chan, Y.; Lehecha, T.; Phillips, L.; Schmitt, A.; Sethian, J.D. Reflected shock experiments on the equation-of-state properties of liquid deuterium at 100–600 GPa (1–6 Mbar). *Phys. Plasma* **2001**, *8*, 2281–2286. [CrossRef]
211. Bonev, S.A.; Militzer, B.; Galli, G. Ab initio simulations of dense liquid deuterium: Comparison with gas-gun shock-wave experiments. *Phys. Rev. B Condens. Matter* **2004**, *69*, 014101. [CrossRef]
212. Laboratory, L.L.N.; Bastea; Zaug, J. Material behavior insight comes as a nanoshock. Available online: https://www.llnl.gov/news/material-behavior-insight-comes-nanoshock (accessed on 1 November 2022).
213. Campanella, B.; Legnaioli, S.; Pagnotta, S.; Poggialini, F.; Palleschi, V. Shock Waves in Laser-Induced Plasmas. *Atoms* **2019**, *7*, 57. [CrossRef]
214. Urtiew, P.A. Effect of shock loading on transparency of sapphire crystals. *J. Appl. Phys.* **1974**, *45*, 3490–3493. [CrossRef]
215. Celliers, P.M.; Loubeyre, P.; Eggert, J.H.; Brygoo, S.; McWilliams, R.S.; Hicks, D.G.; Boehly, T.R.; Jeanloz, R.; Collins, G.W. Insulator-to-Conducting Transition in Dense Fluid Helium. *Phys. Rev. Lett.* **2010**, *104*, 184503. [CrossRef]
216. Bass, J.D.; Svendsen, B.; Ahrens, T.J. The Temperature of Shock Compressed Iron. In *Elastic Properties and Equations of State*; Wiley: Hoboken, NJ, USA, 1988; pp. 532–541.
217. Pakhal, H.R.; Lucht, R.P.; Laurendeau, N.M. Spectral measurements of incipient plasma temperature and electron number density during laser ablation of aluminum in air. *Appl. Phys. B* **2008**, *90*, 15–27. [CrossRef]
218. Nellis, W.J. Dynamic compression of materials: Metallization of fluid hydrogen at high pressures. *Rep. Prog. Phys.* **2006**, *69*, 1479–1580. [CrossRef]
219. Babuel-Peyrissac, J.P.; Fauquignon, C.; Floux, F. Effect of powerful laser pulse on low Z solid material. *Phys. Lett. A* **1969**, *30*, 290–291. [CrossRef]
220. Nellis, W.J. Adiabat-reduced isotherms at 100 GPa pressures. *High Pressure Res.* **2007**, *27*, 393–407. [CrossRef]
221. Grujicic, M.; Runt, J.; Sr, J.T. Molecular Dynamics (MD) and Coarse Grain Simulation of High Strain-Rate Elastomeric Polymers (HSREP). In *Elastomeric Polymers with High Rate Sensitivity*; Barsoum, R.G., Ed.; William Andrew Publishing: Oxford, UK, 2015; pp. 187–232.
222. Zhang, Q.B.; Braithwaite, C.H.; Zhao, J. Hugoniot equation of state of rock materials under shock compression. *Phil. Trans. R. Soc. A* **2017**, *375*, 20160169. [CrossRef]
223. Celliers, P.M.; Bradley, D.K.; Collins, G.W.; Hicks, D.G.; Boehly, T.R.; Armstrong, W.J. Line-imaging velocimeter for shock diagnostics at the OMEGA laser facility. *Rev. Sci. Instrum.* **2004**, *75*, 4916–4929. [CrossRef]
224. Cooper, M.A.; Specht, P.E.; Trott, W.M. Measuring three-dimensional deformation with surface-imaging ORVIS. *J. Phys. Conf. Ser.* **2014**, *500*, 182008. [CrossRef]
225. Evans, W.J.; Yoo, C.-S.; Lee, G.W.; Cynn, H.; Lipp, M.J.; Visbeck, K. Dynamic diamond anvil cell (dDAC): A novel device for studying the dynamic-pressure properties of materials. *Rev. Sci. Instrum.* **2007**, *78*, 073904. [CrossRef]
226. Su, L.; Shi, K.; Zhang, L.; Wang, Y.; Yang, G. Static and dynamic diamond anvil cell (s-dDAC): A bidirectional remote controlled device for static and dynamic compression/decompression. *Matter Radiat. Extremes* **2021**, *7*, 018401. [CrossRef]
227. Yan, J.; Liu, X.; Gorelli, F.A.; Xu, H.; Zhang, H.; Hu, H.; Gregoryanz, E.; Dalladay-Simpson, P. Compression rate of dynamic diamond anvil cells from room temperature to 10 K. *Rev. Sci. Instrum.* **2022**, *93*, 063901. [CrossRef]
228. Smith, J.S.; Sinogeikin, S.V.; Lin, C.; Rod, E.; Bai, L.; Shen, G. Developments in time-resolved high pressure x-ray diffraction using rapid compression and decompression. *Rev. Sci. Instrum.* **2015**, *86*, 072208. [CrossRef]
229. Velisavljevic, N.; Sinogeikin, S.; Saavedra, R.; Chellappa, R.S.; Rothkirch, A.; Dattelbaum, D.M.; Konopkova, Z.; Liermann, H.P.; Bishop, M.; Tsoi, G.M.; et al. Time-resolved x-ray diffraction and electrical resistance measurements of structural phase transitions in zirconium. *J. Phys. Conf. Ser.* **2014**, *500*, 032020. [CrossRef]
230. Cauble, R.; Phillion, D.W.; Hoover, T.J.; Holmes, N.C.; Kilkenny, J.D.; Lee, R.W. Demonstration of 0.75 Gbar planar shocks in x-ray driven colliding foils. *Phys. Rev. Lett.* **1993**, *70*, 2102–2105. [CrossRef]
231. Zheng, X.; Song, Y.; Zhao, J.; Tan, D.; Yang, Y.; Liu, C. Nanosecond time-resolved Raman spectroscopy of molecular solids under laser-driven shock compression. *Chem. Phys. Lett.* **2010**, *499*, 231–235. [CrossRef]
232. Duffy, T.S.; Ahrens, T.J. Sound velocities at high pressure and temperature and their geophysical implications. *J. Geophys. Res. Solid Earth* **1992**, *97*, 4503–4520. [CrossRef]
233. Fratanduono, D.E.; Millot, M.; Kraus, R.G.; Spaulding, D.K.; Collins, G.W.; Celliers, P.M.; Eggert, J.H. Thermodynamic properties of $MgSiO_3$ at super-Earth mantle conditions. *Phys. Rev. B* **2018**, *97*, 214105. [CrossRef]
234. Ichiyanagi, K.; Takagi, S.; Kawai, N.; Fukaya, R.; Nozawa, S.; Nakamura, K.G.; Liss, K.-D.; Kimura, M.; Adachi, S.-i. Microstructural deformation process of shock-compressed polycrystalline aluminum. *Sci. Rep.* **2019**, *9*, 7604. [CrossRef]
235. Johnson, J.D. Bound and estimate for the maximum compression of single shocks. *Phys. Rev. E* **1999**, *59*, 3727–3728. [CrossRef]
236. Nellis, W.J.P.W. Bridgman's contributions to the foundations of shock compression of condensed matter. *J. Phys. Conf. Ser.* **2010**, *215*, 012144. [CrossRef]
237. Kadobayashi, H.; Ohnishi, S.; Ohfuji, H.; Yamamoto, Y.; Muraoka, M.; Yoshida, S.; Hirao, N.; Kawaguchi-Imada, S.; Hirai, H. Diamond formation from methane hydrate under the internal conditions of giant icy planets. *Sci. Rep.* **2021**, *11*, 8165. [CrossRef]

238. Kraus, D.; Vorberger, J.; Pak, A.; Hartley, N.J.; Fletcher, L.B.; Frydrych, S.; Galtier, E.; Gamboa, E.J.; Gericke, D.O.; Glenzer, S.H.; et al. Formation of diamonds in laser-compressed hydrocarbons at planetary interior conditions. *Nat. Astron* **2017**, *1*, 606–611. [CrossRef]
239. Benedetti, L.R.; Nguyen, J.H.; Caldwell, W.A.; Liu, H.; Kruger, M.; Jeanloz, R. Dissociation of CH_4 at high pressures and temperatures: Diamond formation in giant planet interiors? *Science* **1999**, *286*, 100–102. [CrossRef] [PubMed]
240. Hirai, H.; Konagai, K.; Kawamura, T.; Yamamoto, Y.; Yagi, T. Polymerization and diamond formation from melting methane and their implications in ice layer of giant planets. *Phys. Earth Planet. Inter.* **2009**, *174*, 242–246. [CrossRef]
241. Showrilu, K.; Jyothirmai, C.; Sirisha, A.R.N.L.; Sivakumar, A.; Sahaya Jude Dhas, S.; Martin Britto Dhas, S.A. Shock wave-induced defect engineering on structural and optical properties of crown ether magnesium chloride potassium thiocyanate single crystal. *J. Mater. Sci. Mater. Electron.* **2021**, *32*, 3903–3911. [CrossRef]
242. Paulus, W.S.; Rahman, I.A.; Jalar, A.; Othman, N.K.; Ismail, R.; Wan Yusoff, W.Y.; Abu Bakar, M. The Relationship between XRD Peak Intensity and Mechanical Properties of Irradiated Lead-Free Solder. *Mater. Sci. Forum* **2017**, *888*, 423–427. [CrossRef]
243. Ahlam, M.A.; Ravishankar, M.N.; Vijayan, N.; Govindaraj, G.; Upadhyaya, V.; Prakash, A.P.G. The effect of Co-60 gamma irradiation on optical properties of some nonlinear optical (NLO) single crystals. *J. Opt.* **2012**, *41*, 158–166. [CrossRef]
244. Sivakumar, A.; Victor, C.; Nayak, M.M.; Dhas, S.A.M.B. Structural, optical, and morphological stability of ZnO nano rods under shock wave loading conditions. *Mater. Res. Express* **2019**, *6*, 045031. [CrossRef]
245. Thomas, R.; Davidson, P.; Rericha, A.; Recknagel, U. Discovery of Stishovite in the Prismatine-Bearing Granulite from Waldheim, Germany: A Possible Role of Supercritical Fluids of Ultrahigh-Pressure Origin. *Geosciences* **2022**, *12*, 196. [CrossRef]
246. Ackerson, M.R. Trace and Minor Elements in Garnet and Quartz: Novel Approaches to Understanding Crustal Evolution. Ph.D. Thesis, Rensselaer Polytechnic Institute, Ann Arbor, MI, USA, 2015.
247. Guarguaglini, M.; Hernandez, J.A.; Okuchi, T.; Barroso, P.; Benuzzi-Mounaix, A.; Bethkenhagen, M.; Bolis, R.; Brambrink, E.; French, M.; Fujimoto, Y.; et al. Laser-driven shock compression of "synthetic planetary mixtures" of water, ethanol, and ammonia. *Sci. Rep.* **2019**, *9*, 10155. [CrossRef]
248. Arumugam, S.; Sathiyadhas, S.J.D.; Michael, J.; Pichan, K.; Muthu, S.P.; Perumalsamy, R.; Sathiyadhas Amalapusham, M.B.D. Investigation on the impact of xylenol orange dye on the growth and properties of unidirectional grown KDP crystals for photonic applications. *J. Cryst. Growth* **2019**, *523*, 125154. [CrossRef]
249. Kohn, E. Harsh Environment Materials. In *Comprehensive Microsystems*; Gianchandani, Y.B., Tabata, O., Zappe, H., Eds.; Elsevier: Oxford, UK, 2008; pp. 131–181.
250. Wackerle, J. Shock-Wave Compression of Quartz. *J. Appl. Phys.* **1962**, *33*, 922–937. [CrossRef]
251. Kraus, D.; Ravasio, A.; Gauthier, M.; Gericke, D.O.; Vorberger, J.; Frydrych, S.; Helfrich, J.; Fletcher, L.B.; Schaumann, G.; Nagler, B.; et al. Nanosecond formation of diamond and lonsdaleite by shock compression of graphite. *Nat. Commun.* **2016**, *7*, 10970. [CrossRef]
252. Kurdyumov, A.V.; Britun, V.F.; Yarosh, V.V.; Danilenko, A.I.; Zelyavskii, V.B. The influence of the shock compression conditions on the graphite transformations into lonsdaleite and diamond. *J. Superhard Mater.* **2012**, *34*, 19–27. [CrossRef]
253. Thapliyal, V.; Alabdulkarim, M.E.; Whelan, D.R.; Mainali, B.; Maxwell, J.L. A concise review of the Raman spectra of carbon allotropes. *Diamond Relat. Mater.* **2022**, *127*, 109180. [CrossRef]
254. Saha, P.; Annamalai, N.; Guha, A.K. Synthetic Quartz Production and Applications. *Trans. Indian Ceram. Soc.* **1991**, *50*, 129–135. [CrossRef]
255. Knudson, M.D.; Desjarlais, M.P. Shock Compression of Quartz to 1.6 TPa: Redefining a Pressure Standard. *Phys. Rev. Lett.* **2009**, *103*, 225501. [CrossRef]
256. Grieve, R.A.F.; Langenhorst, F.; Stöffler, D. Shock metamorphism of quartz in nature and experiment: II. Significance in geoscience*. *Meteorit. Planet. Sci.* **1996**, *31*, 6–35. [CrossRef]
257. Hicks, D.G.; Boehly, T.R.; Celliers, P.M.; Bradley, D.K.; Eggert, J.H.; McWilliams, R.S.; Jeanloz, R.; Collins, G.W. High-precision measurements of the diamond Hugoniot in and above the melt region. *Phys. Rev. B* **2008**, *78*, 174102. [CrossRef]
258. De Carli, P.S.; Milton, D.J. Stishovite: Synthesis by Shock Wave. *Science* **1965**, *147*, 144–145. [CrossRef]
259. Beason, M.T.; Pauls, J.M.; Gunduz, I.E.; Rouvimov, S.; Manukyan, K.V.; Matouš, K.; Son, S.F.; Mukasyan, A. Shock-induced reaction synthesis of cubic boron nitride. *Appl. Phys. Lett.* **2018**, *112*, 171903. [CrossRef]
260. Pan, Z.; Sun, H.; Zhang, Y.; Chen, C. Harder than Diamond: Superior Indentation Strength of Wurtzite BN and Lonsdaleite. *Phys. Rev. Lett.* **2009**, *102*, 055503. [CrossRef]
261. Kennedy, J.P.; Williams, L.; Bridges, T.M.; Daniels, R.N.; Weaver, D.; Lindsley, C.W. Application of Combinatorial Chemistry Science on Modern Drug Discovery. *J. Comb. Chem.* **2008**, *10*, 345–354. [CrossRef] [PubMed]